

1 Global mapping of RNA-chromatin contacts reveals a 2 proximity-dominated connectivity model for ncRNA-gene 3 interactions

4 **Charles Limouse¹, Owen K. Smith^{2,†}, David Jukam^{1,†}, Kelsey A. Fryer^{1,3},**
5 **William J. Greenleaf³, and Aaron F. Straight^{1,*}**

6 ¹Department of Biochemistry, Stanford University, Stanford, California, USA

7 ²Department of Chemical And Systems Biology, Stanford University, Stanford, California, USA

8 ³Department of Genetics, Stanford University, Stanford, California, USA

9 [†]These authors contributed equally.

10 *To whom correspondence should be addressed: Aaron F. Straight, astraight@stanford.edu

11 Abstract

12 Non-coding RNAs (ncRNAs) are transcribed throughout the genome and provide regulatory inputs to gene
13 expression through their interaction with chromatin. The genomic targets and regulatory mechanisms of
14 most ncRNAs remain unknown. Using chromatin-associated RNA sequencing (ChAR-seq) we obtained
15 a global map of RNA-chromatin interactions, transcriptome and genome-wide, in human embryonic stem
16 cells and definitive endoderm. We defined the overall architecture of the RNA-chromatin interactome
17 that encompasses all long non-coding RNAs, intronic RNAs, as well as unannotated RNAs derived from
18 regulatory elements, transposable elements, and intergenic regions. We show that the interactome is
19 cell state specific, involves functionally diverse classes of RNAs, and can be accurately predicted by a
20 simple model accounting for RNA expression and distance to their DNA targets. We show that nearly all
21 ncRNAs exclusively interact with genes in close three-dimensional proximity to their transcription locus. We
22 identified a small number of RNAs that deviate from that behavior and interact with many loci across the
23 genome. By relating the changes in the interactome during differentiation to changes in gene expression,
24 we demonstrate that activation or repression of individual genes is unlikely to be controlled by the activity
25 of a single ncRNA.

26 Introduction

27 Cell identity is determined by the precise execution of lineage-specific gene expression programs¹.
28 These programs are controlled by coordinated signals from regulatory DNA sequences, transcription
29 factors, histone modifications and variants, and 3D genome organization. The role of RNAs in
30 modulating these programs is increasingly appreciated^{2,3}. Many different RNAs bind chromatin,
31 collectively termed here chromatin-associated RNAs (caRNAs). These include long non-coding RNA
32 (lncRNAs)^{4,5}, heterogeneous nuclear RNAs (hnRNAs)^{6,7}, enhancer-RNAs (eRNAs)^{8,9,10}, transposable
33 element (TE)-derived RNAs^{11,12,13,14}, and other chromatin enriched RNAs (cheRNAs)^{15,16}. Yet, the
34 function of these RNAs on chromatin remains largely unknown.

35 Several examples have demonstrated that lncRNAs can orchestrate complex regulatory circuits.
36 For example, XIST is a core regulator of X-chromosome inactivation¹⁷, and KCNQ1OT1 mediates
37 allele-specific silencing of a group of imprinted genes near its locus^{18,19}. With advances in genomics
38 methods, the proposed regulatory roles of caRNAs have expanded to include RNA species other than
39 lncRNAs. For example, eRNAs can affect expression of neighboring genes through modulation of RNA
40 polII elongation^{20,21}, or recruitment of transcription coregulators^{22,23}. Nascent pre-mRNAs can interact
41 with chromatin architectural proteins and locally regulate chromatin compaction^{6,24}, and TE-derived RNAs
42 can silence immune response genes and hamper the T-cell effector functions²⁵. Furthermore, many
43 proteins involved in controlling chromatin state^{26,27,28,29,30} and topology^{31,23} have RNA-binding activity,
44 establishing a putative mechanistic link between caRNA and gene regulation. Despite these examples
45 and general models, which caRNAs have gene regulatory roles and the mechanisms through which they
46 act is not well understood³².

47 Our ability to understand transcription regulation by caRNAs is hampered by one key gap in our
48 knowledge: we do not know, for all but a select few RNAs, the genomic loci where these RNAs act.
49 This knowledge gap makes it challenging to unravel the network of interactions between caRNAs and
50 genes. Furthermore, this network of interactions is likely highly complex. The number of caRNAs
51 greatly exceeds that of proteins. Annotated lncRNAs alone represent ~20,000 RNAs (Gencode v29),
52 and the number of regulatory elements is estimated to be over 900,000^{33,34}. Although the transcriptional
53 activity of these regulatory elements hasn't been fully characterized, conservative estimates based on a
54 subset of promoters and enhancers from FANTOM5 indicate at least 100 000 such elements generate
55 RNAs^{35,1,36}. Transcription of both lncRNAs^{37,38} and regulatory elements^{9,39,36,35} exhibit strong tissue
56 specificity such that the ncRNA-gene interaction network is also likely cell-state dependent, although this
57 remains to be experimentally tested. More generally, pervasive transcription outside of protein-coding
58 regions provides a large sequence space with potential regulatory activity^{40,41,42}. Given the suggested
59 associations between sequence or expression variations in lncRNAs, TE-derived RNA, or eRNAs and
60 human health, characterization of the network of human caRNA-gene interactions at the full transcriptome
61 scale represents an important goal^{43,25,44,45,46}.

62 Here, we used chromatin-associated RNA sequencing (ChAR-seq) to map the RNA-chromatin interactome
63 in H9 embryonic stem cells and definitive endoderm^{47,48,49}. From these data we characterize the global
64 architecture of this interactome, present a model which predicts the majority of RNA-DNA chromatin
65 interactions based on RNA-target distance, and highlight RNAs deviating from this model. Finally, we
66 generate an all-to-all caRNA-gene interaction network linking every gene to the set of caRNAs with
67 which it interacts based on physical proximity. Our network encompasses lncRNAs, as well as many
68 unannotated intergenic RNAs and could help prioritize specific caRNAs for future functional validation
69 studies. Finally, we analyzed the dynamics of the interactome during differentiation to shed light on the
70 potential mechanisms by which caRNAs may regulate genes.

71 Results

72 To detect caRNAs and map their interactions with the genome, we applied our recently developed assay,
73 ChAR-seq^{48,47,49}, a proximity-ligation method that captures and sequences RNA-DNA contacts across

74 the genome and transcriptome (Fig. 1a). We performed ChAR-seq in human H9 embryonic stem cells
75 (ES) before and after differentiation into definitive endoderm (DE) to understand how changes in the
76 caRNA-chromatin interaction network might relate to activation or repression of cell-state specific genes
77 upon differentiation. We validated our cell differentiation system by qPCR against cell-state marker
78 genes and immunostaining, which revealed pure (>99%) ES and DE cell populations (Extended Data
79 Fig. 1a,b) ⁵⁰.

80 We performed deep sequencing of the ChAR-seq libraries to obtain over 900 million reads per cell state
81 across 2 replicates. We computationally split each read into a RNA- and a DNA-derived sequence and
82 selected reads that passed stringent quality filters with both the RNA and DNA sequences mapping to
83 unambiguous loci (Supplementary Fig. 1 and Methods). We thereby obtained the RNA identity and
84 genomic target for nearly 200 million unique RNA-DNA contacts (Supplementary Fig. 2).

85 We first analyzed the global composition of the caRNA population. We observed a high level of RNAs
86 derived from introns (Fig. 1b), which likely reflects the capture of RNA during nascent transcription while the
87 RNA is tethered to chromatin through polymerase, or other forms of chromatin retention of introns such as
88 interaction with RNA binding proteins ^{51,52,4,53}. caRNAs were enriched for non-coding RNAs, including long
89 non-coding RNAs (lncRNAs) and other short non-coding RNAs encompassing several functionally distinct
90 subtypes of RNAs such as small nuclear RNAs (snRNAs) and small nucleolar RNAs (snoRNAs; Fig. 1c,
91 Extended Data Fig. 2a). Overall, caRNAs are highly diverse, with as many RNAs represented at above 0.1
92 Fragment Per Million (FPM, ~10 reads at our sequencing depth) in the caRNA transcriptome as in the total
93 RNA transcriptome (Extended Data Fig. 2 b-d, Supplementary Tables 1,2). To normalize the composition
94 of the caRNA population to expression levels, we assigned each RNA a chromatin association score, which
95 we defined as its relative abundance in the ChAR-seq versus total RNA-seq data (Methods). We found
96 that nearly all introns and half of all ncRNAs, including half of the ~5,000 lncRNAs detected, had over
97 3-fold enrichment on chromatin, in agreement with prior characterizations of caRNA ^{54,16}, indicating that
98 ncRNAs tend to have nuclear or chromatin localization (Fig. 1d, Extended Data Fig. 3a-d, Supplementary
99 Table 3). Thus, while lncRNAs are often considered prime candidates for potential chromatin regulatory
100 roles ^{3,34}, our data indicate that non-intronic regions of lncRNAs only constitute approximately 3% of the
101 caRNA population, and less than 1% when excluding the top 10 most abundant lncRNAs. This result
102 prompted us to perform a broad analysis of RNA-DNA interactions, including all caRNAs, rather than to
103 focus exclusively on lncRNAs.

104 Because the chromatin association patterns and potential chromatin activity of exon- and intron-derived
105 RNAs might be distinct, we generated separate RNA-DNA contact maps for exons and introns (Fig. 1e).
106 Our RNA-DNA contact maps were highly reproducible (Extended Data Fig. 4a) and showed high
107 correlation between replicates and lower correlation between cell states, indicating that the interactome
108 is dynamic during differentiation (Extended Data Fig. 4b). In both ES and DE cells and across exons
109 and introns, we uncovered several features of the RNA-DNA interactome mirroring those described in
110 our prior work on *Drosophila melanogaster* and by others ^{55,48,56,54,57}. First, we noted a higher density
111 of intrachromosomal compared to interchromosomal RNA-DNA contacts, reminiscent of the properties
112 observed at the DNA level by Hi-C ⁵⁸, and likely reflecting the chromatin organization into chromosome
113 territories ⁵⁹. Furthermore, the average contact frequency between an RNA and a genomic target dropped
114 sharply as a function of the distance between the RNA locus and the target, with an average ~100-fold
115 lower contact density 50-100 kb away from the transcription locus compared to at the transcription locus
116 (Extended Data Fig. 4c). Finally, we observed 3 classes of RNAs with distinct chromatin association
117 patterns (Fig. 1). i) Many RNAs localized predominantly at or near their transcription locus. ii) Another
118 set of RNAs, including the MALAT1 RNA, localized across the genome, as previously observed ^{56,60}.
119 iii) The third class of RNA, which includes XIST, is characterized by chromatin interactions across a
120 single chromosome. The localization of XIST across the X chromosome was more apparent in DE cells,
121 concomitant with its transcriptional activation and the initiation of X chromosome inactivation during early
122 embryonic development ⁶¹. We confirmed by RNA fluorescence in situ hybridization microscopy that the
123 nuclear localization of select RNAs from these classes was consistent with their classification by ChAR-seq

124 (Extended Data Fig. 5). Altogether, these RNA-chromatin interactomes identify numerous RNAs in
 125 different functional classes that dynamically reorganize dependent upon cell state and demonstrate that
 126 most caRNAs remain associated with chromatin near their sites of synthesis.

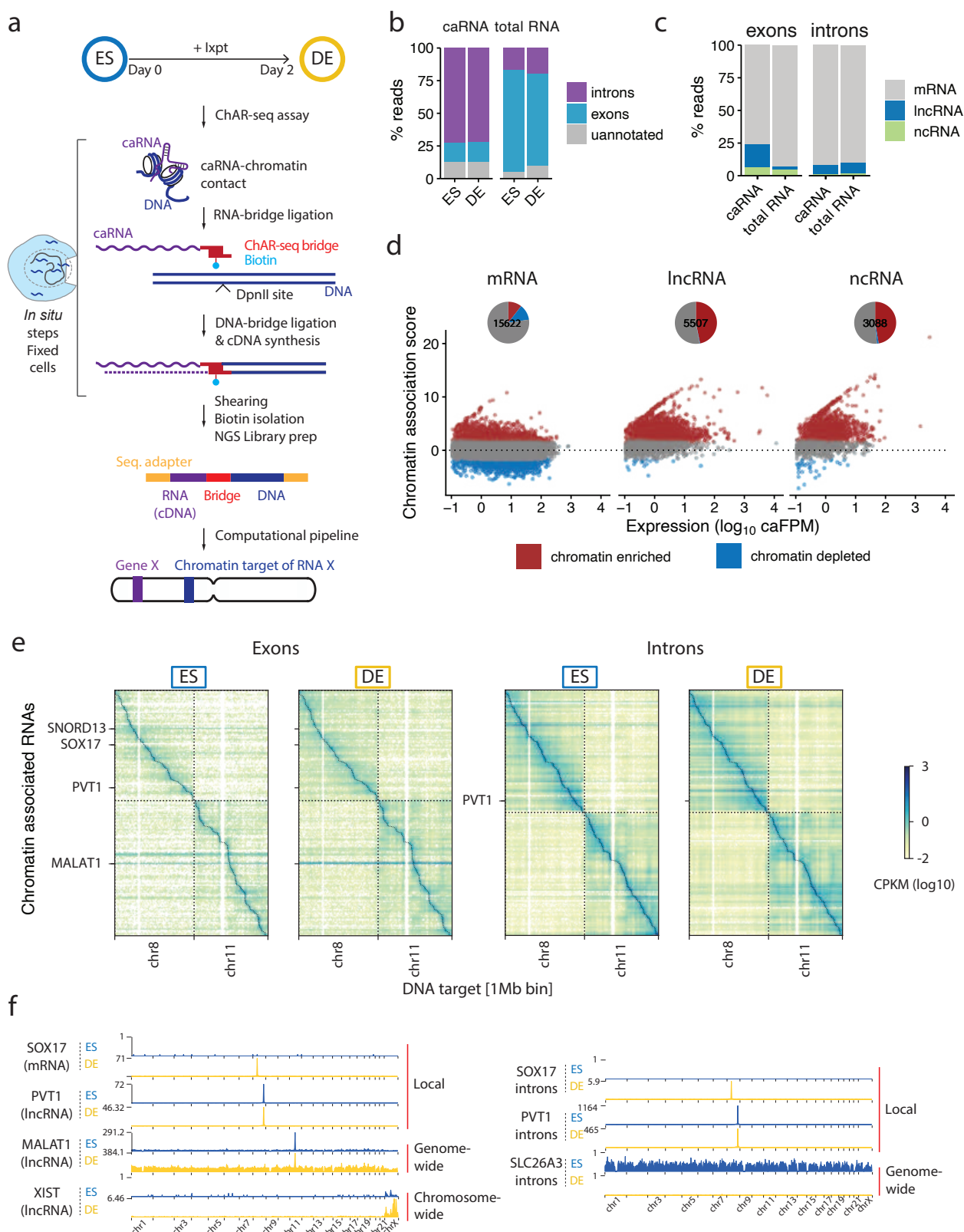


Figure 1. Global mapping of RNA-chromatin interactions during stem cell differentiation. **a**, Schematic of the strategy used to map RNA-DNA contacts across the transcriptome and genome by ChAR-seq, highlighting the key steps of the workflow. **b-c**, Composition of the caRNAs identified by ChAR-seq compared to the total RNA population determined by total RNA sequencing.

Figure 1 (previous page). d, Scatter plots showing the chromatin association scores for individual RNAs originating from annotated exons, as a function of the RNA level in the caRNA population. Chromatin enriched and depleted RNAs were determined using DESeq2 (FDR 0.05, fold change threshold 3x). Pie charts summarize the fraction of chromatin enriched and chromatin depleted RNA in each functional RNA type. The numbers within each pie chart indicate the total number of RNAs in that category. **e**, RNA-DNA contact maps in ES and DE cells for the top 200 most abundant caRNAs (according to their mean expression in ES and DE cells) on Chr7 and Chr8. Maps are displayed at a resolution of 1 RNA per row and 1 Mbp of genome space per column. Color represents contact density defined as the number of contacts between an RNA and a genomic bin, normalized for sequencing-depth and size of the genomic bin (CPKM: Contacts Per Kb in target genomic region per Million reads). Contacts made by exonic and intronic RNAs are shown in left and right maps, respectively. **f**, Interaction profiles along the genome for SOX17, PVT1, MALAT1 and XIST exons, and for SOX17, PVT1 and SLC26A3 introns, illustrating 3 major classes of interaction profiles: RNAs localized predominantly near their transcription locus (SOX17, PVT1 exons and introns), spreading across a single chromosome (XIST), and across the genome (MALAT1, SLC26A3 introns)

127 **A highly cell-state specific population of unannotated RNAs localizes on chromatin**

128 Strikingly, we identified unannotated RNAs that did not overlap with any known genes (as of Gencode
129 v29) in 14% of all RNA-DNA contacts—a proportion similar to that of exons for annotated RNAs (Fig. 1b).
130 To further characterize the nature of these unannotated transcripts, we used the StringTie *de novo*
131 transcriptome assembler to identify individual transcription units (Fig. 2a)⁶². We uncovered 78,314
132 data-inferred transcription loci, which we hereafter refer to as unannotated transcribed loci (UTLs), 30,442
133 of which were above 0.1 FPM in ES or DE cells (Extended Data Fig. 6a-b, Supplementary Table 4). Thus,
134 the number of UTLs is comparable to the 22,475 (resp. 23,832) Gencode transcripts with exons (resp.
135 introns) above 0.1 FPM. We examined the genomic context of these RNAs and noted that UTLs were
136 composed of distinct functional classes of RNAs (Fig. 2b). Some UTLs were immediately continuous with
137 the 3' end of active genes (e.g., UTL69162), thus likely originating from transcriptional read-through, as
138 reported in prior studies^{63,64}. Other UTLs overlapped at their 5' end with known regulatory elements (e.g.,
139 UTL69163), as indicated by their relative proximity to gene transcription start sites (TSSs), high ATAC-seq
140 signal, H3K27ac levels, and their overlap with annotations from the ENCODE Registry of Regulatory
141 Elements v3³³. These *cis* regulatory element-derived RNAs (CRE-derived RNAs) are likely a mixture of
142 enhancer RNAs (eRNAs) and promoter upstream RNAs^{65,66}. Another subset of RNAs mostly overlapped
143 or were immediately downstream of TEs (e.g., UTL69657), in agreement with prior studies showing that
144 TEs are a source of RNAs that associate with chromatin^{11,25,12}. A fourth and fifth category of UTLs did
145 not have any of the above features but were either antisense to known genes or localized in intergenic
146 regions. Finally, some UTLs had sequence similarity with known transfer RNAs (tRNAs), snRNAs other
147 small RNAs and tended to be very abundant (Supplementary Fig. 3). These UTLs may derive from either
148 mature or unprocessed transcripts from these tRNAs and snRNAs complete gene units⁶⁷. Guided by
149 these observations, we classified the UTLs based on their proximity to the 3' or 5' ends of genes, their
150 overlap with transposable elements, snRNAs, or tRNAs, and their overlap with *cis* regulatory elements
151 annotated in the Encode Registry of Regulatory Elements³³, yielding 7 categories of unannotated RNAs
152 (Methods). We found that on average across ES and DE cells, ~32% of the reads coming from UTLs
153 were classified as readthrough RNAs and ~27% as *cis* regulatory element-derived (Fig. 2c). Over 60% of
154 the CRE-derived RNAs were from enhancer elements (Extended Data Fig. 6a). Four percent of the UTL
155 reads were repeat-derived transcripts, roughly evenly distributed between LTR, SINE, and LINE elements
156 (Fig. 2c, Extended Data Fig. 6a). Overall, the expression levels of UTLs were low, but similar to those of
157 lncRNAs (Extended Data Fig. 2b, Extended Data Fig. 6b-c).

158 Although these RNAs were present in the total RNA population, chromatin association score analysis
159 indicated that all categories of UTLs were enriched on chromatin (Fig. 2d, Extended Data Fig. 6a,
160 Supplementary Fig. 4). We also found that UTLs were highly cell-state specific in both the total RNA
161 and caRNA populations (Fig. 2e). 15-49% of UTLs were up- or down-regulated in the caRNA and total
162 RNA populations compared to only ~12% for mRNAs and lncRNAs. The high cell state specificity of
163 CRE-derived RNAs in particular is consistent with prior studies³⁷. We generated RNA-DNA contact
164 maps specifically for UTLs, which showed patterns similar to those observed for exonic and intronic RNAs

165 (Fig. 2f). We found both UTLs which were locally restricted near their locus and UTLs that spread across
 166 the whole genome (Fig. 2g). This result prompted us to perform a broad analysis of RNA-DNA interactions,
 167 including all caRNAs, rather than to focus exclusively on lncRNAs.

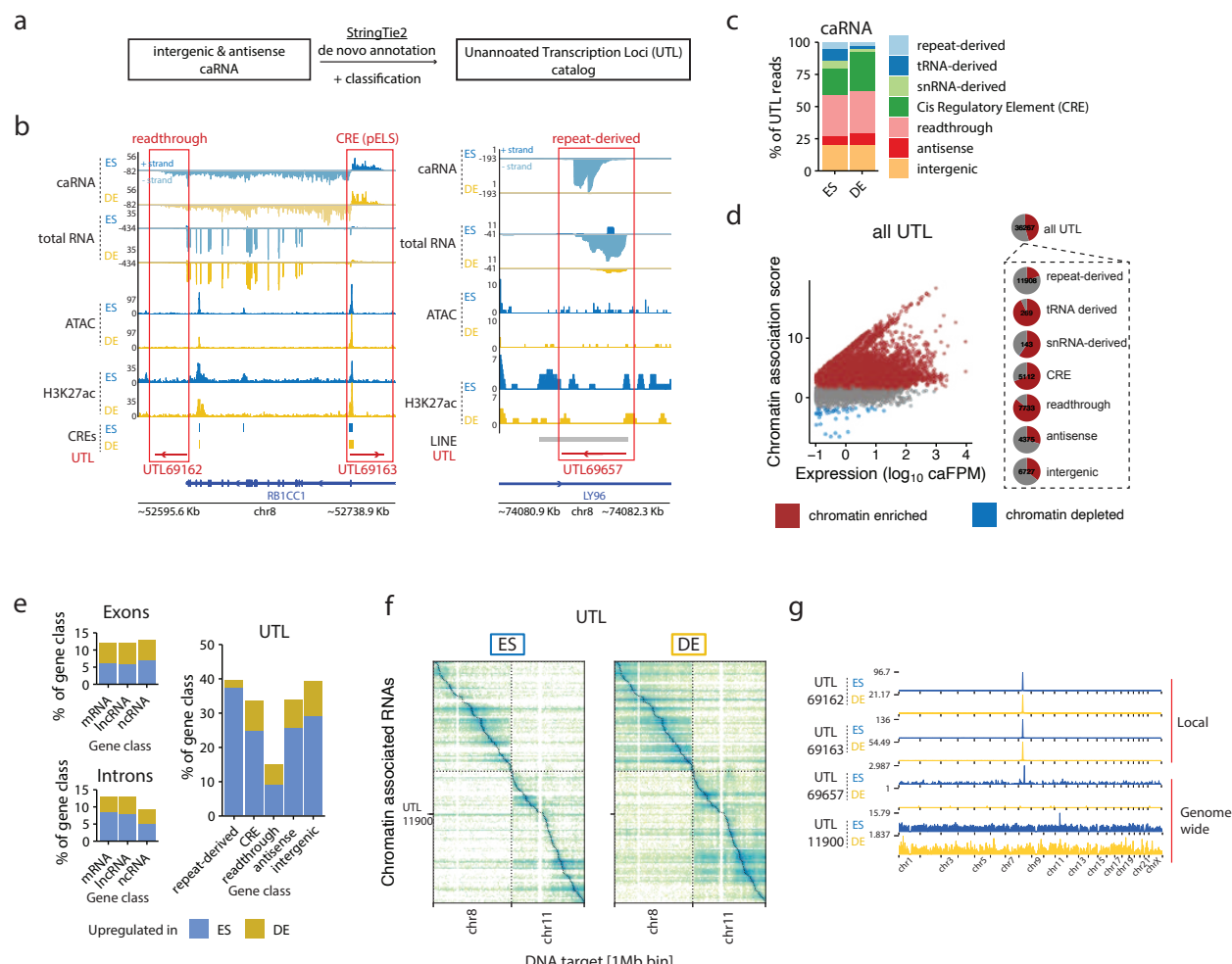


Figure 2. Cell state specific unannotated RNAs make up a large fraction of the caRNAs. **a**, Schematic of the method used to catalog unannotated RNAs by identifying transcription units using StringTie2. **b**, Genome tracks showing the chromatin context of 3 representative unannotated transcription loci (UTL). Left panel: UTL69162 and UTL69163, respectively downstream and antisense to RB1CC1 are classified as a readthrough RNA and CRE-derived RNAs. Right panel: UTL69657 is classified as a repeat-derived RNA due to its overlap with a LINE element. In both left and right panels, the top 2 tracks display the strand-specific genome coverage of the RNA-derived side of the ChIP-seq reads in ES and DE replicate 1 (+ strand ES in dark blue, - strand ES in light blue, + strand DE in dark yellow, - strand DE in light yellow). Next two tracks display the strand-specific genome coverage of the total RNA-seq data. **c**, Relative composition of the chromatin-associated UTLs in the 7 annotation classes. **d**, Scatter plots showing the chromatin association scores for individual UTLs and their abundance in the caRNA population. Chromatin enriched and depleted UTLs were determined using DESeq2 (FDR 0.05, fold change threshold 3x). Pie charts summarize the fraction of chromatin enriched and chromatin depleted UTLs in each category. Numbers within each pie chart indicate the total number of RNAs in that category. **e**, Percentage of genes upregulated and downregulated in DE vs ES cells in the caRNA transcriptome and for each RNA category. Up- and downregulated RNAs were identified using DESeq2 (FDR 0.05, fold change threshold 3x). **f**, RNA-DNA contact maps in ES and DE cells for the top 200 most abundant UTLs on Chr7 and Chr8, displayed at a resolution of 1 RNA per row and 1 Mbp of genome space per column. **g**, Genome-scale chromatin interaction profiles of 4 UTLs showing similar localization patterns as annotated RNAs.

168 **RNA-DNA interactome dynamics is driven by caRNAs transcription dynamics rather than**
 169 **relocalization of caRNAs**

170 We next quantified the dynamics of the RNA-chromatin interactome during ES-DE cell differentiation.
 171 To identify cell-state dependent interactions, we binned the DNA contacts of each RNA into 100 kb or

172 1 Mb intervals and performed a quantitative analysis analogous to differential expression analysis to
173 obtain the fold change of each contact in ES versus DE cells and its associated statistical significance
174 (Methods). In total, after filtering the data to only include contacts with at least 10 counts in at least two
175 samples, we tested ~100,000 exon-chromatin contacts, ~300,000 UTL-chromatin contacts, and 1.6 million
176 intron-chromatin contacts (all at 100 kb resolution) for differential representation in ES vs DE cells. The
177 corresponding maps are shown in Fig. 3a. While we observed few dynamic RNA-chromatin interactions far
178 from the RNA transcription locus (TL) in the exon and UTL maps, zooming in on a 10 Mb window around
179 each RNA TL at 100 kb resolution revealed widespread changes in the interactome for all categories of
180 RNAs. At 100 kb resolution ~2% of interactions involving exons and ~7% of interactions involving introns
181 were up- or down-regulated in DE versus ES cells (Fig. 3b). More substantial changes were observed at
182 a lower resolution of 1 Mb per genomic bin (Supplementary Fig. 6).

183 The interactome dynamics during differentiation may be driven by three non-mutually exclusive effects
184 (Fig. 3c). First, an RNA may increase or decrease in overall abundance, resulting in proportionally
185 increased or decreased binding levels on chromatin. Second, an RNA may modulate its affinity for
186 chromatin, for instance, through RNA modifications or through changes in affinity with RNA-binding
187 proteins mediating its interaction with chromatin. Third, an RNA may relocalize from one genomic site
188 to another. The first two modes of dynamics would result in similar binding profiles in ES vs DE cells, albeit
189 with an overall scale shift in binding levels. In contrast, the third mode implies changes in the RNA binding
190 pattern to chromatin.

191 To test these models, we first compared the chromatin association score of each RNA in ES versus DE
192 cells. Remarkably, the chromatin association scores remained mostly unchanged during differentiation,
193 particularly for lncRNAs, with only 35 lncRNAs showing evidence of changes in their chromatin affinity
194 (Fig. 3d, left panel, Supplementary Table 3). Surprisingly, a larger fraction of UTLs compared to ncRNAs
195 (~8% of CRE-derived UTLs and ~5% of intergenic and antisense UTLs) had significant changes in their
196 chromatin association score between ES and DE cells (Fig. 3d, right panel), yet this fraction remained
197 small. Thus, while individual RNAs show different propensities to interact with chromatin, this propensity
198 is not modulated during differentiation and seems to be a property of the RNA itself. This result rules out
199 model 2 for the majority of caRNAs.

200 Next, we examined whether the dynamics of specific interactions between an RNA and a chromatin locus
201 can be explained by the transcriptional dynamics of the RNA itself. We compared the true differential
202 contact maps to differential contact maps that would be observed if the frequency of each RNA-DNA
203 contact was proportional to the total abundance of the corresponding RNAs in the caRNA population
204 (Methods). These two differential interaction maps were highly similar (Fig. 3e). We further quantified
205 the differences between these maps by identifying specific RNA-DNA contacts whose frequency changes
206 between ES vs DE cells at a greater level than explained by the changes in RNA expression (Methods).
207 We found no such contacts in the exon-DNA interactome and a negligible number of them in the UTL-DNA
208 interactome (Fig. 3f). Thus, the bulk of the changes in the RNA-DNA interactome appear to rely on
209 transcription level regulation and expression differences in ES vs DE, rather than on modulation of an
210 RNA's affinity for chromatin or changes in an RNA's contacts to different DNA binding sites.

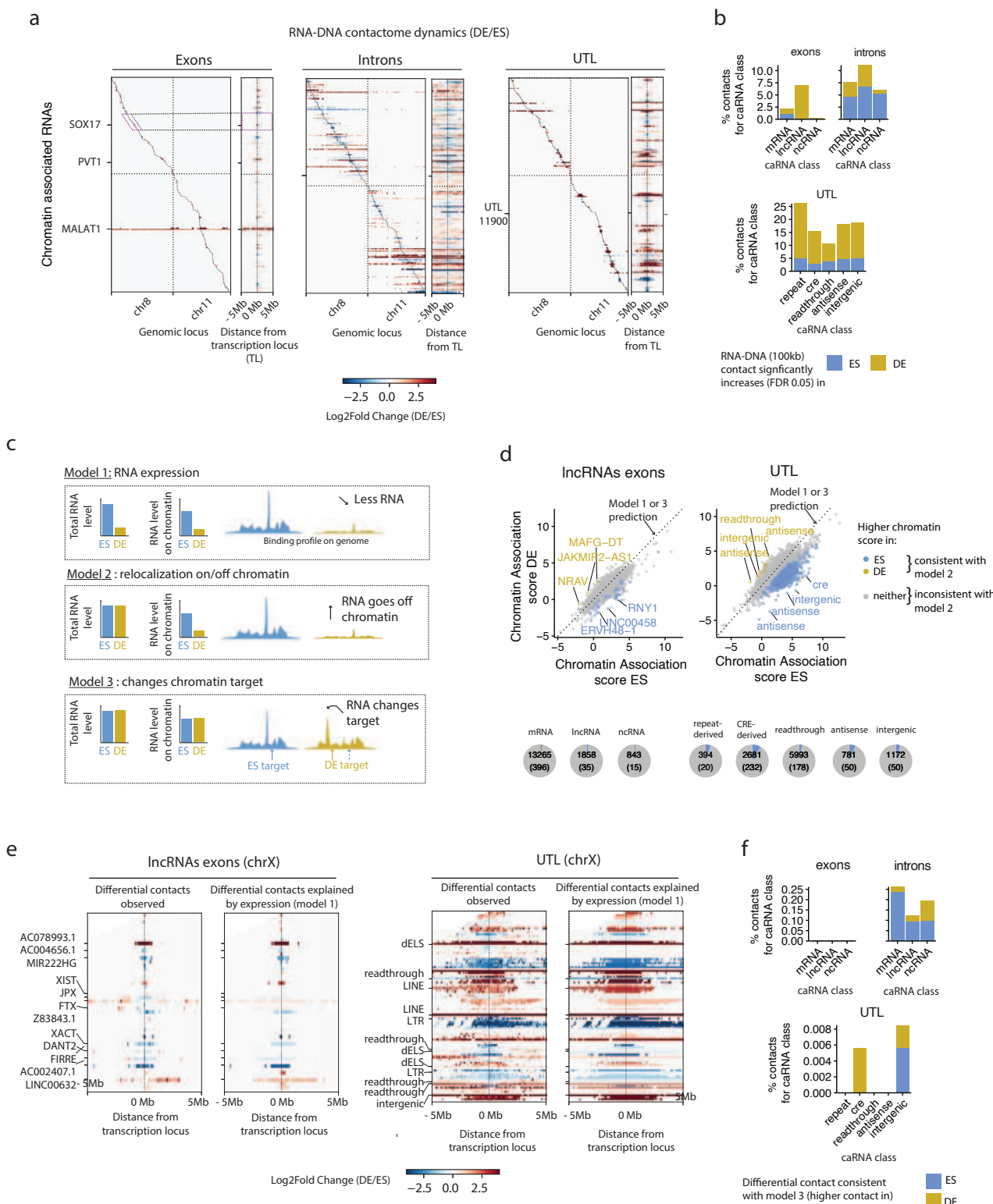


Figure 3. The RNA-DNA interactome dynamics is controlled at the transcription level. **a**, Differential contact maps showing the changes in the RNA-DNA interactome on Chr7 and Chr8 during cellular differentiation, for the same top 200 most abundant exonic RNAs, intronic RNAs, and UTLs as those shown Fig. 1e and Fig. 2f. For each RNA category, the left map shows the log₂ fold change (LFC) in the frequency of each RNA-DNA contact, as computed by DESeq2 (shrunken LFC estimates, see Methods). x-axis resolution is 1 Mb as in Fig. 1e and Fig. 2f. The right map shows a zoom in of the left differential map in a 10 Mb window centered at the Transcription Locus (TL) of each caRNA, and displayed with an x-axis resolution of 100 kb.

Figure 3 (previous page). b, Quantification by RNA class of the percentage of interactions upregulated in DE or ES cells amongst all interactions tested in that class (interactions with >10 counts in at least one replicate in ES or DE), at 100 kb resolution (bottom panel). **c**, Schematic of 3 models that can explain changes in the DNA contact profile of an RNA during differentiation. **d**, Scatter plot showing the chromatin association score for individual lncRNAs exons (left panel) and UTLs (right panel) in ES versus DE cells. All of the lncRNAs with an expression level above 0.1 FPM in both ES and DE cells are shown. Pie charts summarize the fraction of RNAs with significantly higher chromatin association in ES or DE cells (fold change >3, FDR 0.05), and for each RNA class. Numbers within the pie charts indicate the total number of RNAs in that class (FPM >0.1) and the number of RNAs with differential chromatin association. **e**, Differential contact maps observed versus those explained by transcription dynamics only for the 50 most abundant lncRNAs (left) and UTL (right) on ChrX. Labeled genes are the top 12 most abundant genes. x-axis resolution is 100 kb, and a 10 Mb window centered around each RNA TL is shown. **f**, Percentage of differential interaction not explained by differential RNA expression, at 100 kb resolution, relative to the total number of interactions tested within the RNA class.

211 A select number of RNAs interact with the genome broadly

212 We hypothesized that the dynamic RNA-DNA interactome contains a mixture of i) functional interactions
213 linked to regulatory activity of the RNA on chromatin, and ii) coincidental interactions due to transient
214 proximity of the RNA to chromatin, for instance, during nascent transcription or diffusion within the nucleus.
215 We thus analyzed the contact patterns of individual RNAs to detect features consistent with functional
216 interaction, beginning with features at the chromosome scale. The nuclear speckle-associated lncRNA,
217 MALAT1, and the XIST RNA are two well studied lncRNAs which act to regulate gene expression broadly
218 across the genome or throughout the X chromosome^{68,60,69}. Yet, it is not known which other RNAs have
219 similar widespread interaction patterns on chromatin.

220 To systematically identify all RNAs with genome- or chromosome-wide associations, which we termed
221 type I and type II RNAs (Fig. 4a), respectively, we developed two metrics, a *trans*-delocalization and
222 a *cis*-delocalization score (Fig. 4b and Methods). The *trans*-delocalization score of an RNA is loosely
223 defined as the ratio of the number of contacts on chromosomes other than its chromosome of origin
224 (*trans* chromosomes) to the number of contacts on its own chromosome. This score thus quantifies
225 the tendency for an RNA to be found on *trans* chromosomes (Supplementary Table 5). Similarly, the
226 *cis*-delocalization score assesses the tendency for an RNA to spread far from its locus on its source
227 chromosome by quantifying the ratio of the number of contacts over 1 Mb away from its transcription
228 locus (TL) to the number of contacts within 10 Mb of its TL (Supplementary Table 6). We reasoned that
229 type I RNAs must have high *trans*- and *cis*-delocalization scores, while type II RNA must have a high
230 *cis*-delocalization score but a low *trans*-delocalization scores. Thus, although other patterns may yield
231 high delocalization scores (e.g. an RNA which targets a single locus on a *trans*-chromosome may have a
232 large *trans*-delocalization score), we can use these metrics to screen for candidate RNAs with type I and
233 type II patterns. We found that lncRNAs with large *trans*-delocalization scores (Fig. 4e, left panel) included
234 MALAT1, the pTEFb-associated RNA, 7SK, and the telomerase RNA component, TERC, which all have
235 established genome-wide chromatin regulatory functions, thus validating our approach^{70,71,72}.

236 We found that functionally distinct classes of RNAs had different distributions of delocalization scores
237 (Fig. 4c, Supplementary Table 7). lncRNAs had a wide range of delocalization scores, with a distribution of
238 scores that mirrored those of mRNAs. In contrast, snRNAs, snoRNAs, tRNA-derived and snRNA-derived
239 UTLs had globally high *cis*- and *trans*-delocalization scores, indicating that RNAs in these classes interact
240 with loci throughout their source chromosome and across the whole genome. We observed the opposite
241 behavior for CRE-derived RNAs and, to an even greater extent, for readthrough RNAs, which had mostly
242 negative *cis*- and *trans*-delocalization scores, demonstrating that these RNAs tend to remain near their
243 locus of origin. We also noted a negative-shifted distribution of delocalization scores for introns of both
244 mRNAs and lncRNAs (Extended Data Fig. 7a). For ~77% of individual lncRNAs and 97% of individual
245 mRNAs, the *trans*-delocalization scores of their introns were lower than those of their exons (Extended
246 Data Fig. 7b-c). Thus, introns tend to remain in closer proximity to their source locus.

247 Interestingly, repeat-derived RNAs had globally high *cis*- and *trans*-delocalization scores in ES cells

248 and low *cis*- and *trans*-delocalization scores in DE cells (Fig. 4c). Thus, in ES cells specifically, many
249 repeat-derived RNAs tend to localize away from their locus.

250 To identify RNAs with extreme association scores, we applied an empirical Bayes method using mRNAs
251 as a training set, which essentially identified RNAs in the 5% right-tail or the 5% left-tail of the mRNA
252 score distribution (Methods). We thus created a complete catalog of RNAs with candidate chromosome-
253 or genome-wide association patterns, and another catalog of RNAs that remain localized within a 10 Mb
254 window around their transcription locus or on their own chromosome, which we termed ultra-localized
255 RNAs (from a *cis*- or *trans*-chromosomal perspective, Supplementary Table 8). As expected, >50% of
256 snRNAs, snoRNAs, tRNAs, and snRNAs were classified as *trans*-delocalized and >70% of readthrough
257 RNAs were classified as ultra-localized (Fig. 4d). Surprisingly, out of 1,289 ncRNAs above 1 FPM with
258 sufficient signal to compute delocalization scores (Methods), we detected only 22 lncRNAs (1.7%) with
259 *cis*- or *trans*-delocalized patterns in either ES or DE cells (Fig. 4d and Fig. 4e, left panel). In contrast, we
260 found (excluding tRNA-derived and snRNA-derived UTLs) 60 UTLs in DE cells and 836 UTLs in ES cells
261 and with *cis*- or *trans*-delocalization patterns, including 349 repeat-derived RNAs, and several hundreds of
262 intergenic or CRE-derived UTLs (Extended Data Fig. 8a). Our catalog of lncRNAs contained the known
263 broadly acting RNAs discussed above.

264 Importantly, we discovered new candidate lncRNAs with potential genome-wide regulatory functions,
265 including the mitochondrial RNA processing endoribonuclease RNA, RMRP, which is implicated in
266 rRNA maturation^{73,74,46}, the Ribonuclease P RNA Component H1, RPPH1, which is involved in tRNA
267 processing^{75,76}, two isoforms of the Vault RNA, VTRNA1-1 and VTRNA1-3, and a large number of UTLs.
268 We validated the delocalization score analysis by directly examining the ChAR-seq signal of these RNAs,
269 which revealed their association across the genome (Fig. 4f). The delocalization of these RNAs was
270 not explained by their abundance. Although MALAT1, 7SK, and RMRP were highly abundant, other
271 delocalized RNAs were all below 10 FPM. Furthermore, many abundant ncRNAs had low delocalization
272 scores (Fig. 4e, right panel). To confirm that the broad patterns detected by our delocalization score
273 approach were not random or due to non-specific interactions, we performed metagene analysis centered
274 on select genomic features. We detected enrichment of snRNAs at RNAPII occupancy loci (Extended
275 Data Fig. 8b), where MALAT1 and 7SK were also enriched, consistent with the role of these RNAs in
276 cotranscriptional splicing and transcriptional elongation^{68,70}. Together, our data show that broadly localized
277 RNAs are rare amongst annotated lncRNAs, but we detected a large repertoire of UTLs with potential
278 global chromatin regulatory roles, specifically in ES cells.

279 While our catalog contained RNAs that were identified as significantly delocalized in *cis* but not in *trans*,
280 we noted that amongst these RNAs, all but XIST also had a high *trans*-delocalization scores, albeit
281 below the FDR threshold for classification as *trans*-delocalized. Generally, across all RNAs, the *cis*-
282 and *trans*-delocalization scores were strongly correlated, indicating that RNAs that localize broadly on
283 their own chromosomes also interact broadly with the rest of the genome (Fig. 4g). Remarkably, XIST
284 was the only exception to this rule and was the only RNA which was simultaneously delocalized in *cis*
285 and ultralocalized in *trans*, consistent with its known localization throughout its source chromosome X
286 (Fig. 4g-h). We concluded that XIST is unique in these cell types in its ability to interact with an entire
287 chromosome while being excluded from other chromosomes.

288 We next looked at changes in RNA delocalization in different cell states. We found that the delocalization
289 scores were highly correlated between ES and DE cells, even for RNAs that were differentially abundant
290 across cell states (Fig. 4h). We thus concluded that the extent to which an RNA interacts with chromatin
291 far from its transcription locus or on *trans* chromosomes is encoded in the RNA itself or the position of its
292 transcription locus relative to other genomic features, rather than post-transcriptionally regulated.

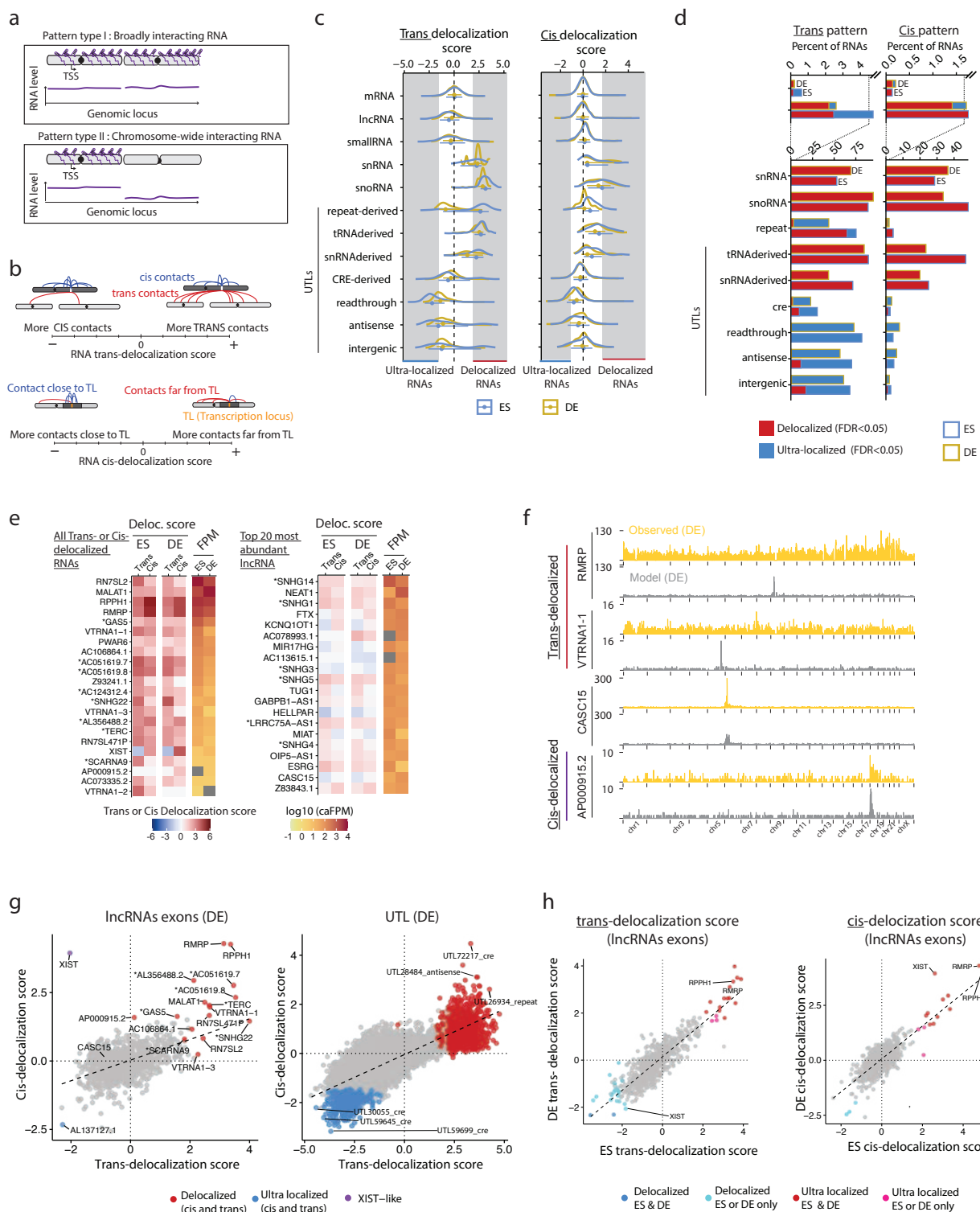


Figure 4. A select population of caRNAs interact with the genome broadly. **a**, Schematic of the two types of binding patterns identified in this analysis: type I) RNAs localized across the genome (*trans*-delocalized RNAs), type II) RNAs localized throughout their source chromosome but absent on other chromosomes (*cis*-delocalized RNAs).

Figure 4 (previous page). b, Schematic definition of the *trans*- and *cis*-delocalization scores. The *trans*-delocalization score quantifies the number of DNA contacts an RNA makes on chromosomes other than its source chromosome (*trans* contacts), relative to the number of contacts on its source chromosome (*cis* contacts). The *cis*-delocalization score quantifies the number of DNA contacts an RNA makes over 10 Mb away from its transcription locus (TL), relative to the number of contacts within 10 Mb of its TL. **c**, Distribution of *trans*- (left) and *cis*- (right) delocalization scores by class of RNA for exons and UTLs (introns are shown in Extended Data Fig. 7a). **d**, Fraction of RNAs within each class identified as either delocalized or ultralocalized in regard to its *trans*- (left) or *cis*-chromosomal contacts (right). **e**, Left: list of all lncRNAs identified as *cis* or *trans*-delocalized in either ES or DE cells and candidate RNAs for type I or type II patterns. Heat maps show the RNA *cis* and *trans* delocalization scores in ES and DE cells, and their abundance in the carNA population. Right: *cis*- and *trans*-delocalization scores for the 20 most abundant lncRNAs (excluding those identified as *cis*- or *trans*-delocalized). **f**, Chromatin interaction profiles for two examples of *cis*-delocalized RNAs (RMRP, VTRNA1-1), one example of *cis*-delocalized RNAs (AP000915.2), and one non-delocalized RNA (CASC15). Yellow track shows the observed ChAR-seq signal. Gray track shows the predicted interaction profile based on the generative model and empirical Bayes model. **g**, Scatter plot showing the *cis*- versus *trans*-delocalization score for individual lncRNAs in ES cells (left), and UTLs in DE cells (right, excludes tRNA-derived and snRNA-derived UTLs). Colored data points indicate RNAs classified as delocalized (in either *cis* or *trans*), ultralocalized (in both *cis* and *trans*), and RNAs with XIST-like behavior. Black line shows the linear regression output. **h**, Scatterplots showing the *trans*- (left) and *cis*-delocalization scores (right) for individual lncRNAs in DE versus ES cells. Black lines show linear regression output

293 **RNA-DNA contacts occur in the vicinity of the transcription locus**

294 Engreitz et al. proposed a dichotomization of RNA-chromatin interactions into proximity-driven and
295 affinity-driven interactions². The former describes interactions occurring in a 2D or 3D distance bounded
296 region around the transcription locus, without specificity for particular loci within that region. The latter
297 describes RNA targeting well-defined loci, irrespective of their distance to the RNA locus. Some ncRNAs
298 have been proposed to have affinity-driven interactions and regulate transcription or 3D organization of
299 chromatin at their target loci^{77,78,79,3}. These data motivated us to search the interactome for contact
300 patterns in which an RNA shows discrete peaks in its localization profile that are not explained by proximity
301 to its locus (Fig. 5a, top panel, hereafter referred to as Type III patterns). Because standard genomic peak
302 finding tools like MACS2⁸⁰ are not appropriate for ChAR-seq data, we instead developed a generative
303 model, which predicts the RNA-DNA interactome based on 3 features: 1) the total abundance of each RNA
304 on chromatin, 2) a DNA-locus bias which models the propensity for an RNA to be captured at this locus,
305 independently of the identity of that RNA, and 3) the distance between each RNA transcription site and its
306 DNA target loci (Fig. 5b and Supplementary Methods). As anticipated, the DNA-locus bias correlated with
307 ATAC-seq, likely due to a combination of biological factors such as fewer RNA-DNA interactions existing
308 in compact chromatin, and technical biases related to accessibility of the ChAR-seq bridge molecule. The
309 DNA-locus bias also correlated with nuclear speckle proximity as measured by TSA-seq⁸¹, revealing a
310 possible increased affinity for diffusing RNAs towards nuclear speckles. We trained our generative model
311 on mRNAs, as we reasoned that most mRNAs should not have defined chromatin targets. We then used
312 our final model to generate a “predicted” contact pattern for each RNA, which effectively provides a null
313 hypothesis representing “neutral” patterns, where an RNA interacts exclusively and non-specifically with
314 neighboring loci due to diffusion (Fig. 5a, model track). Thus, positive deviations from the prediction
315 (more contacts in the observed data compared with the model prediction) provide evidence for peak-like
316 interactions in type III patterns.

317 In both ES and DE cells and for exons, introns, and UTLs, our simple generative model produced
318 RNA-DNA contact maps qualitatively similar to true ChAR-seq RNA-DNA contacts maps (Fig. 5d).
319 Correlations between observed and predicted maps were nearly as high as correlations between replicates
320 (Extended Data Fig. 9a). At 100 kb DNA locus resolution and excluding RNAs previously identified as *cis*-
321 or *trans*-delocalized, we identified only ~0.2% of exon and ~0.7% of intron contacts that were not explained
322 by the model, irrespective of whether the RNAs were mRNAs, lncRNAs, or ncRNAs (Fig. 5e and Extended
323 Data Fig. 9b-c). Thus, we detected only 11 and 9 lncRNAs in ES and DE cells, respectively, with exons
324 making contacts in the genome at loci not predicted by our model (Supplementary Table 9). Our model
325 also accurately predicted changes in contact rates during differentiation (Extended Data and Fig 9d). Thus,
326 in contrast with prior studies^{77,79,78}, we found no evidence for type III patterns amongst the entire lncRNA

327 population.

328 Interestingly, in contrast with that of lncRNAs, the interactome of the UTLs differed more substantially from
329 its prediction. Over 1% of contacts, or 3433 and 4986 contacts involving 2283 and 2597 distinct RNAs in
330 ES and DE cells, respectively, showed statistical evidence for affinity-driven interactions (Supplementary
331 Table 9). Readthrough RNAs had the largest number of contacts (2.6%, 2465 contacts in DE) significantly
332 different from the model, and CRE-derived RNAs at ~1% (1514 contacts in DE) significantly different from
333 the model (Extended Data Fig. 9c). This result suggests that many unannotated RNAs, in particular
334 regulatory elements derived RNAs, engage in genomic contacts that cannot be explained by a diffusion
335 process around the transcription locus similar to that of mRNAs.

336 To better understand the nature of these contacts, we examined how far from the RNA transcription
337 locus these contacts occurred (Extended Data Fig. 10a,b). We found the majority of the significant
338 contacts made by UTL occurred within 100 kb of their locus (51%, 4316 contacts across ES and DE
339 cells). The percentage of significant contacts within 100 kb was highest amongst readthrough RNAs
340 (69%-74%). In contrast, introns of annotated RNAs tended to show deviations from the predicted patterns
341 at larger distances. Indeed we found that only 17% of contacts from introns that were not predicted by
342 the model occurred within 100 kb of their locus, whereas 88% occurred between 100 kb and 10 Mb.
343 The difference in distances between RNA loci and their significant DNA contacts between annotated
344 intron RNAs and unannotated RNAs suggests different types of interactions might be regulating RNA
345 spread across chromosomes. Because these length scales are reminiscent of those involved in genome
346 organization at the levels of TADs and A/B compartments^{82,83,84}, we examined the relationship between
347 the RNA localization patterns and the 3D organization of the genome.

348 **The 3D genome organization enables contacts between RNAs and distal chromatin loci**

349 To examine how the 3D organization of the genome affects the localization patterns of individual RNAs
350 on chromatin, we focused on the example of a small ~50 kb TAD on chr4q25, which is nested inside a
351 larger 100 kb TAD (Fig. 5g). Two genes are located at the inner boundary of the small and large TADs:
352 AC106864, an uncharacterized lncRNA, and the LARP7 gene, which is antisense to AC106864 and is
353 highly transcribed in ES cells. We examined the binding profile of AC106864 on chr4 and found that most
354 of the contacts of this RNA were within a few kb of its locus. Yet we also observed two side peaks, labeled
355 L1 and L2, that coincided with the other edge of the small and large TAD, respectively. In contrast, our
356 generated model predicted a small peak at L1 (likely due to high accessibility of this locus as revealed by
357 ATAC-seq) and no signal at L2. The Fold Difference signal of the observed data over the model confirmed
358 that the 2 peaks at L1 and L2 were not explained by a simple diffusion of the AC106864 or accessibility
359 biases. Interestingly, Hi-C data showed two corner peaks characteristic of a chromatin loop linking the
360 LARP7 locus with both L1 and L2. This result suggests that AC106864 localization at L1 and L2 might
361 be mediated by the chromatin loop. It is also possible that AC106864 targets these loci through other
362 mechanisms such as base-pairing or association with RBP that are independent of genome folding. Yet
363 this biochemically targeted interaction is unlikely given that the introns of the overlapping mRNA LARP7
364 also have contact peaks at L1 and L2. Together, these data suggest that TAD organization influences the
365 contact patterns of RNAs, and that chromatin looping enables distal RNA-DNA interactions.

366 This observation prompted us to ask whether larger-scale topological organization of the chromosome
367 also influences RNA-DNA contacts (Fig. 5h). ChAR-seq contact maps are naturally asymmetric in that the
368 y-axis maps each row to an individual RNA and the x-axis maps each column to a genomic bin. Thus to
369 compare ChAR-seq to Hi-C data at the chromosome scale, we collapsed one dimension of the Hi-C maps
370 into genes while keeping the other dimension as genomic bins. In these transformed Hi-C maps, each pixel
371 represents the contact frequency between the gene and a cognate DNA bin. We detected in the ChAR-seq
372 maps the same plaid pattern found in Hi-C data resulting from the 3D partitioning of the genome into two
373 major compartments, the A and B compartments, also associated with active and inactive chromatin,
374 respectively⁸⁴. This pattern indicates that any individual caRNA tends to have a specific compartment
375 (either A or B) with which it interacts preferentially. Equivalently, when one caRNA contacts a locus in say

376 the A compartment, it has higher likelihood to contact other loci in the A compartment rather than in the
 377 B compartment. It was not surprising that this pattern was not produced by our generative model, since
 378 only linear distance is encoded in the model. We concluded that A/B compartments also modulate the
 379 long-range interactions of individual RNAs with chromatin.

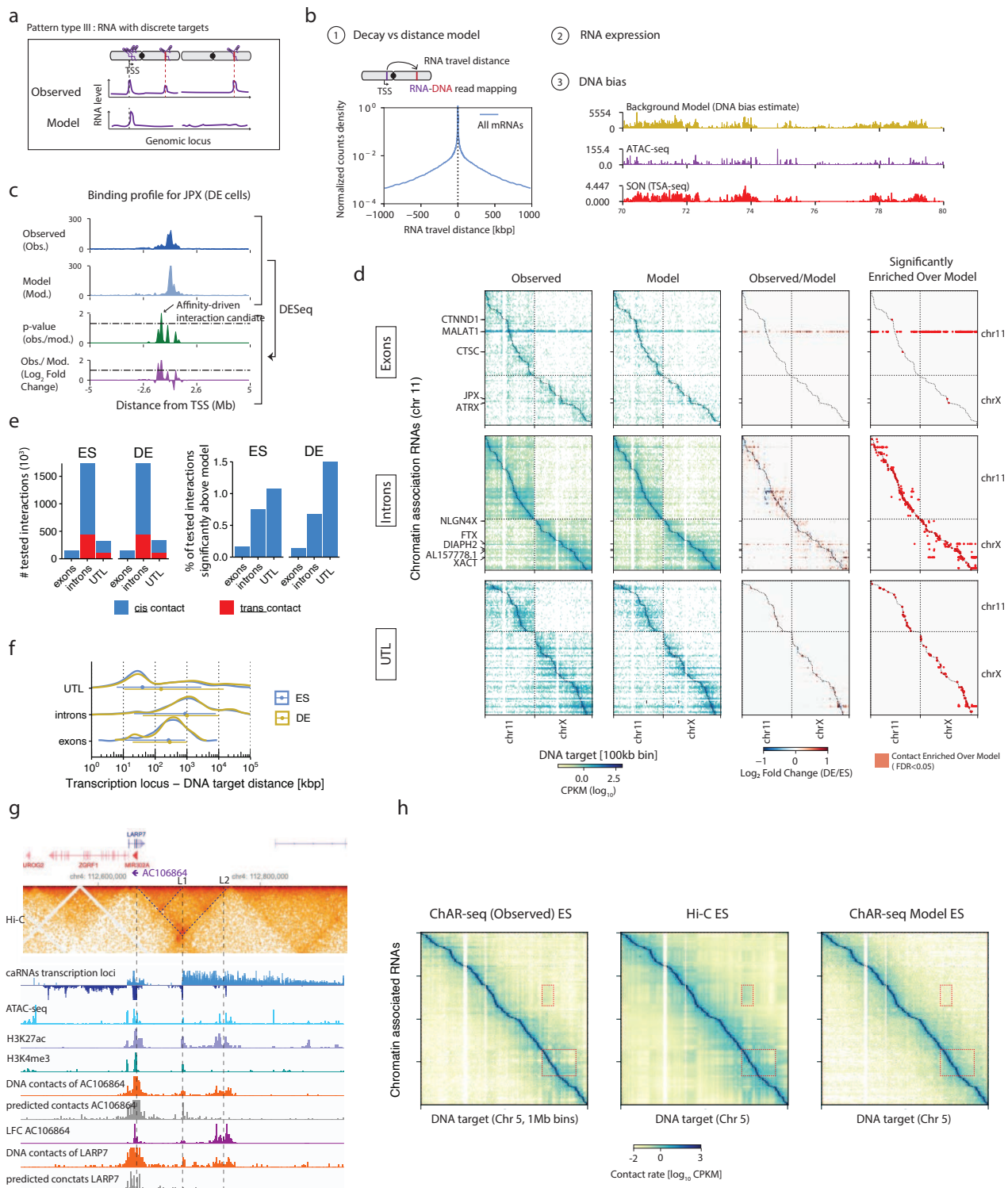


Figure 5. RNA expression and genomic distance determine the RNA-DNA interactome. **a**, Schematic of the type of binding patterns identified in this analysis. An RNA may localize at one or more discrete loci distinct from its transcription site (Pattern type III, top track) or remain in a diffusion constrained region around its locus (neutral RNA, bottom track).

Figure 5 (previous page). b, Components of the generative model used to predict the ChAR-seq maps. The number of contacts observed for an RNA at a DNA locus is proportional to i) an RNA-DNA distance-dependent contact frequency, ii) the abundance of the RNA on chromatin, iii) a target locus dependent bias (DNA-bias, yellow track) which correlates with both ATAC-seq signal (purple track) and nuclear speckle proximity signal (TSA-seq, red track). **c**, Example of a type III pattern with a candidate affinity-driven interaction for the lncRNA JPX in DE cells. The observed and predicted localization of JPX (top two tracks) at 10 kb resolution, and the are compared using DESeq2, yielding a Log₂ fold change (observed over model) and an adjusted p-value track (bottom two tracks). Interactions with an LFC greater than 1.3 and an adjusted p-value smaller than 0.05 are labeled as “candidate affinity driven interaction”. **d**, Observed contact maps, predicted contact maps, and observed over model LFC maps computed using DESeq2 for the top 200 most abundant RNAs originating from exons (top), introns (middle) and UTLs (bottom). x-axis resolution is 100 kb per bin, Y-axis resolution is 1 RNA per bin. Only interactions with at least 10 counts in at least two samples were tested for differences with the model and are shown in the LFC maps. **e**, Number of interactions tested for enrichment over model and proportion of identified candidate affinity-driven interactions by RNA class, in relation to the total number of tested interactions in that RNA class. **f**, Distribution of the RNA-DNA travel distance for interactions significantly above model. The RNA-DNA travel distance is calculated using the mapping coordinates of the RNA and DNA side of the ChAR-seq read (Methods). **g**, Example of long-range RNA-DNA contacts across a chromatin loop at the LARP7 & AC106864 locus in ES cells. ICE normalized Hi-C map (2 kb resolution) is shown at the top. Transcription of LARP7 (expressed from the positive strand) and AC106864 (expressed from the negative strand, shown as negative values) are detected by ChAR-seq (top 2 tracks). The observed (dark orange) and predicted localization pattern (dark grey) of AC106864 on chromatin are shown with the log fold difference between observed and predicted (purple). The observed and predicted localization patterns for LARP7 are shown in light orange and light gray. ATAC-seq, H3K27ac and H3K4me3 tracks are also shown and indicate that L2 has enhancer-like chromatin properties. **h**, Comparison between ChAR-seq and Hi-C at the chromosome scale. Dashed boxes highlight two example regions where the A/B compartments plaid pattern is clearly visible in both Hi-C and ChAR-seq maps

380 **The caRNA-gene interactome preferentially links upregulated caRNAs to upregulated target
381 genes**

382 Our results point to a model where RNA-chromatin association patterns and their dynamics are restricted
383 by i) the caRNA expression level ii) the genomic distance from the RNA locus to the DNA target, iii) the
384 3D chromatin topology. We thus wanted to determine whether this result is compatible with the hypothesis
385 that ncRNAs participate in the regulation of cell-state specific protein-coding genes. We reasoned that
386 RNAs with transcriptional regulatory roles are likely to be found near their cognate gene, where they could
387 modulate local chromatin state, TF binding, RNA polymerase, or the activity of gene-proximal regulatory
388 elements. This colocalization hypothesis is consistent with the better studied ncRNAs with gene regulatory
389 activity, including XIST¹⁷, KCNQ1OT1¹⁸, and HOTAIR⁸⁵. Thus, we defined a “proximal regulatory region”
390 (PRR) around each protein-coding gene, encompassing +10 kb upstream and -90 kb downstream of its
391 TSS, and measured the contact density of each caRNA at the PRR of each gene. Using this approach,
392 we mapped all the physical contacts between the chromatin associated transcriptome and protein-coding
393 genes (hereinafter referred to as the caRNA-gene interactome, Fig. 6a).

394 Consistent with the dynamics of the genome-wide RNA-DNA interactome we previously observed, the
395 caRNA-gene interactome of >1 million contacts was dynamic across differentiation. We detected most
396 of the differential contacts at genes nearby the RNA locus (Fig. 6b). For lncRNAs only, we detected
397 340 differential contacts (~1% of all lncRNA-gene contacts), but these involved only 57 distinct lncRNAs,
398 indicating that a typical single lncRNAs differentially contacts multiple genes (Fig. 6c,d). Also consistent
399 with the global interactome dynamics, the caRNA-gene interactome involving UTLs was more dynamic
400 than that involving annotated RNAs, with up to 20% differential UTL-gene contacts between ES and DE
401 (Fig. 6d).

402 To identify potential regulatory caRNAs and their putative gene targets, we next classified each caRNA and
403 each protein-coding gene as an ES, DE, or stable caRNA or gene, based on whether it was differentially
404 expressed in ES, in DE, or similarly expressed in both cell states (FDR cutoff 0.05, Fold Change cutoff 3).
405 We then examined the statistical associations between the class (ES/DE/stable) of a caRNA, its cognate
406 gene, and their interaction. Fig 6e shows the top 20 most upregulated contacts involving a lncRNA in ES
407 (left panel) or DE (right), along with the cognate lncRNA-gene pair. We noted that nearly all these top 20
408 ES (resp. DE) upregulated contacts involved ncRNAs upregulated in the same state. This result makes

409 sense given our prior findings that the RNA-DNA interactome dynamics is globally driven by transcriptional
410 dynamics. Yet most of the target genes for these differential contacts were not differentially expressed in
411 ES vs DE, suggesting that changes in the caRNA levels at these genes do not affect their expression. We
412 generalized this finding by analyzing across all caRNA-target gene pairs linked by a differential contact,
413 the relationship between the fold change in the contact and the fold change in the expression of the caRNA
414 or of the target gene (Fig. 6f). We found that the fold change in contact rate during ES to DE transition
415 correlated with the fold change of the expression of the source caRNA (Fig. 6f, left panel), but not with that
416 of the target protein coding gene (Fig. 6f, right panel).

417 To further understand the relationship between gene expression and presence of a caRNA in the PRR of
418 a gene, we examined how many cell-state specific contacts are made at cell state-specific genes. This
419 analysis revealed that >97% of cell state specific genes are not contacted by a lncRNAs in a cell state
420 specific manner (Fig. 6g, left panel). Interestingly however, over 50% of these genes are contacted by at
421 least one, and sometimes several UTL specifically in one cell state (and 15% with a CRE), nearly twice
422 as many as genes that are not cell-state specific. Thus, most genes do not require cell-state specific
423 localization of a particular lncRNA in their PRR to alter their expression, but genes whose expression is
424 altered are likely to be contacted by an UTL in a cell-state specific manner. Together, our findings indicate
425 that the presence of an individual ncRNA near the gene TSS does not correlate with the gene transcription.
426 This result does not rule out a regulatory activity of ncRNAs at protein coding genes. Indeed, it is likely
427 that multiple inputs may gate the target gene expression, including chromatin state, transcription factors,
428 and possibly several RNAs, which could wash out average correlations between caRNA-gene interactions
429 and gene transcription.

430 To identify patterns in the interactome that would indicate a regulatory structure, we compared the
431 observed interactome dynamics to that that would be expected should it be independent of the gene
432 expression dynamics (null model). We binned differential contacts in 3 categories: i) positive edges, where
433 the contact dynamics were positively correlated with the target gene dynamics (contacts that increased
434 in ES to genes that increased in ES, or contacts that increased in DE to genes that increased in DE), ii)
435 negative edges (contacts that increased in ES to genes that increased in DE, or contacts that increased
436 in DE to genes that increased in ES), iii) neutral edges (contacts that increased in ES or DE to genes that
437 were neither ES or DE genes).

438 We found that across all categories of caRNAs, the interactome contained up to 1.8 times more positive
439 edges (p -value<0.05 by bootstrap) and up to 1.3 times fewer negative edges (p -value<0.05 by bootstrap)
440 than would be expected for a random interactome under the null model (Fig. 6h,i). Thus, we conclude
441 that although specific RNAs are not sole drivers of transcription activation or silencing at any gene, the
442 architecture of the interactome is consistent with an overall positive regulation, where the presence of
443 caRNAs is generally associated with higher expression of the target genes.

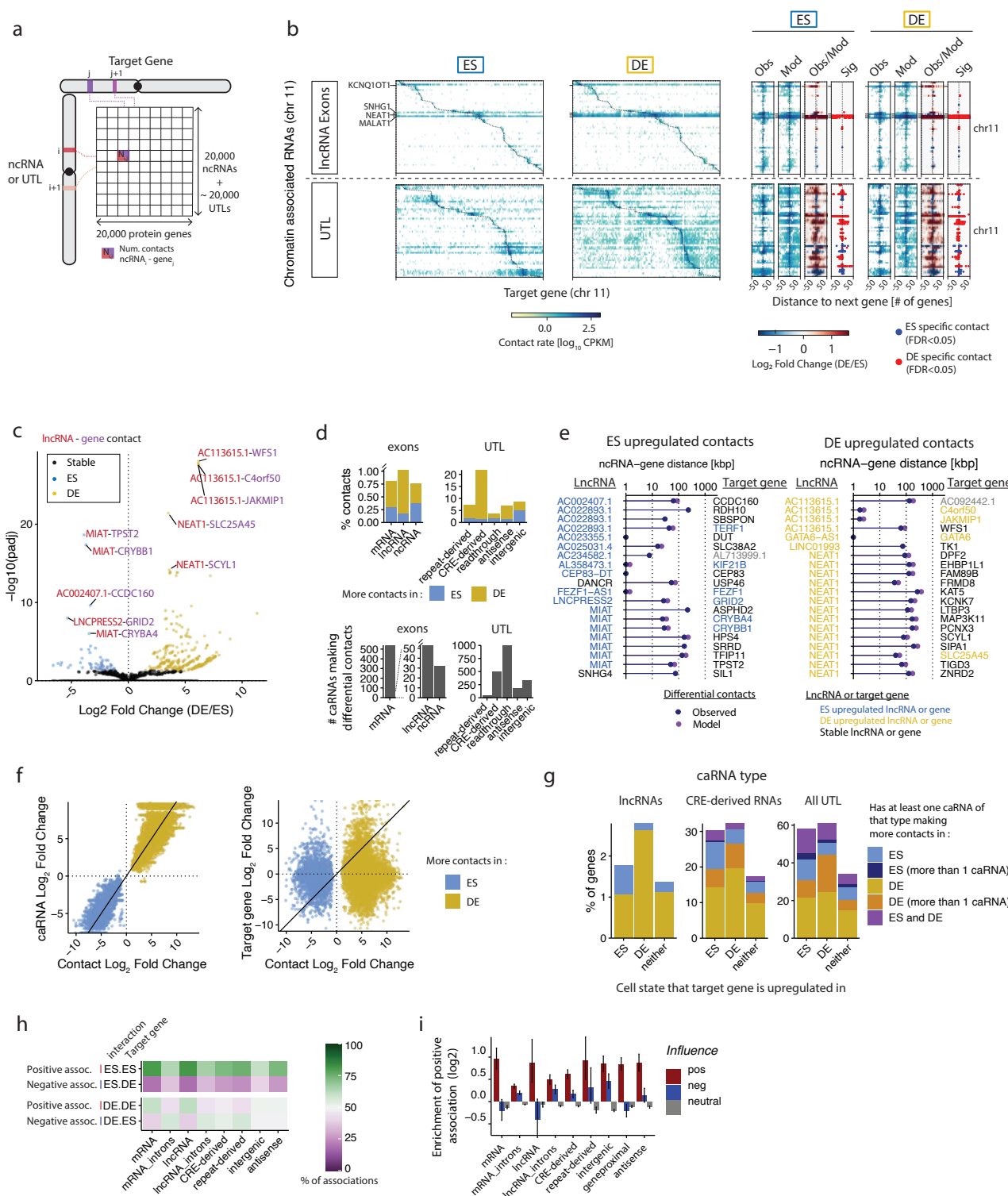


Figure 6. The caRNA-gene interactome preferentially links upregulated caRNAs to upregulated genes. **a**, Abstract representation of the caRNA-gene interactome studied in this analysis and displayed as a contact matrix with one caRNA per row and one protein-coding gene per column. Each matrix entry contains the number of contacts between an ncRNA and the proximal regulatory region (PRR) of a protein coding gene. Only *cis* interactions are shown for simplicity, but *trans* interactions are represented similarly.

Figure 6 (previous page). b, caRNA-gene interactome in ES and DE cells for the 50 most abundant lncRNAs (top) and UTLS (bottom) on Chr11. Narrow maps on the right are zoomed in view of the interactome for 50 protein-coding genes upstream and downstream of each caRNA PRR. Zoomed in maps are shown for the true interactome signal (Obs), the interactome predicted by the generative model (Mod), the \log_2 fold change ($LFC_{obs \text{ over } model}$) of the observed data over model (Obs/Model), and the interactions significantly enriched in the observed data over the model (Sig), namely those with adjusted p -value < 0.05 and $LFC_{obs, model} > 0$, obtained using DESeq2 as described in Fig. 4c-d. Only contacts with at least 10 counts in at least 2 samples were tested for enrichment over model. **c**, Volcano plot showing the differential lncRNA-gene contacts in ES versus DE cells. Each data point is a contact between a lncRNA and the PRR of a protein-coding gene. Volcano plots are shown as contact adjusted p -value versus \log_2 Fold Change in DE versus ES cells ($LFC_{ES, DE}$). Differential contacts are computed as in Fig. 3a, and significant contacts are those with an adjusted p -value < 0.05 . **d**, Quantification of the percentage of cell-state specific contacts for each class of caRNA relative to the number of contacts tested for that class (top), and number of distinct caRNAs involved in these contacts (bottom). Cell-specific contacts were defined as those with an adjusted p -value < 0.05 and $LFC_{ES, DE} > 1.3$. **e**, Top 20 lncRNA-gene contacts upregulated in ES (left) and DE cells (right) in the observed data (blue circles). Most of these contacts are also predicted to be amongst the 20 most upregulated contacts by the generative model (purple circles). **f**, Scatter plots showing for each differential contact the relationship between the change in contact rate during differentiation ($LFC_{ES, DE}$) and the change in the chromatin levels of the involved caRNA (left) and in the expression of the cognate protein coding gene (right). Differential contacts were defined as in d). Only differential contacts involving exons of lncRNAs or UTLS are shown. **g**, Percent of protein-coding genes, targeted by one or more dynamic contact with a lncRNA (left panel), a CRE-derived RNA (middle panel), or any UTL (right panel, excluding tRNA- and snRNA-derived NARs). Protein coding genes are grouped (x-axis) according to whether their expression is upregulated in ES, DE, or stable during differentiation as measured by total RNA-seq (DEseq2, FDR 0.05, fold change threshold 3x). Colors indicate whether the protein coding gene is targeted by a single (light colors) or several (dark colors) caRNAs with which the interaction is upregulated in ES (blue shade) or DE (yellow shade). Some genes are targeted by several caRNAs which include both ES and DE upregulated interactions (purple). **h**, Top two rows: Percentage of interactions upregulated in ES targeting a protein coding gene upregulated in ES, which we define as a positive association, or targeting a protein coding gene upregulated in DE, which we define as a negative association. Bottom two rows: similarly, for interactions upregulated in DE cells. x-axis indicates the caRNA class. **i**, Fold enrichment of the fraction of positive associations in the observed interactome, compared to a randomized interactome, where the differential expression state of the target genes is shuffled. Error bars indicate 95% confidence intervals by bootstrap. Error bars not overlapping with x-axis indicate p -value < 0.05 by bootstrap.

444 Discussion

445 Understanding how caRNAs control chromatin state and transcription is a long-standing problem. To date, 446 only a few RNAs have been linked to specific regulatory functions and the mechanistic details remain 447 debated. In this work, we provide a global view of the RNA-chromatin interactome which complements 448 studies focused on individual RNAs and uncovers general principles governing the architecture of putative 449 ncRNA-gene regulatory networks.

450 First, we show that lncRNAs with promiscuous chromatin interactions are rare. Given that we detected 451 only a handful of lncRNAs with such patterns, it is unlikely that uncharacterized lncRNAs have global 452 regulatory roles, such as those established for 7SK, MALAT1, XIST, or TERC. However, we identified a 453 larger repertoire of unannotated RNAs with broad chromatin interactions which contained many TE-derived 454 RNAs. These data reinforce the idea that transcriptionally active LINE, SINE and LTR may play key 455 roles in chromatin regulation and highlight the necessity to further explore the biology of transposable 456 elements⁸⁶.

457 Second, it is noteworthy that all delocalized lncRNAs but TERC and 2 uncharacterized ncRNAs 458 (VAULT-RNA and AC073335) are known RNA residents of the nucleolus (RMRP, RPPH1, 7SL, most 459 snoRNAs) or nuclear speckles (7SK, MALAT1, most snRNAs). SPRITE, a Hi-C-like method which 460 probes high order chromatin interactions, showed that the 3D genome is organized into 2 major hubs 461 around the nucleolus and nuclear speckles, where abundant long-range and interchromosomal DNA-DNA 462 contacts occur⁸⁷. We hypothesize that the proximity of these RNA loci to the genomic hubs may be 463 important in enabling interactions with dispersed genomic loci. This behavior is reminiscent of XIST, whose 464 location on the X chromosome defines where heterochromatin spreading initiates¹⁷. We speculate that a 465 general principle may underlie these observations, where the interactions of an RNA with chromatin are

466 constrained by the position of their transcription locus relative to other loci or to nuclear domains.

467 Third, we demonstrate unambiguously that no RNA behaves like XIST and localizes throughout its own
468 chromosome while being excluded from other chromosomes. Thus, while XIST sets expectations for
469 ncRNAs regarding their potential roles as regulators of transcription and large genetic networks, XIST
470 appears to be unique in its localization pattern.

471 Fourth, excluding small RNAs such as snRNAs, snoRNAs, tRNAs, and some UTLs as described above,
472 we found no evidence across the non-coding transcriptome for widespread existence of *trans* interactions,
473 or of affinity-driven interactions as defined by Engreitz et al². Indeed, we demonstrated that a simple
474 generative model, encoding only for expression and RNA-DNA distance, accurately predicts the contact
475 patterns for each RNA. Thus, while acknowledging possible false-negatives for lowly expressed RNAs as
476 discussed later, we show that nearly all interactions are proximity-driven. An important implication of our
477 results is that across the non-coding transcriptome, chromatin regulatory activities are essentially limited
478 to nearby genes.

479 Several modes of regulatory activity are compatible with proximity-driven interactions, yet our work brings
480 in important refinements to the proposed models. If a ncRNA serves as a platform to locally recruit
481 histone modifying complexes, as proposed for many lncRNAs, we show that the dimensions of the
482 domain around the RNA transcription locus where this activity occurs is solely determined by the RNA
483 expression. The same local constraints apply if a ncRNA operates via a decoy mechanism, whereby it
484 evicts specific remodeling complexes from chromatin, through competitive or inhibitory associations with
485 these complexes⁸⁸.

486 To our surprise, we observed a general lack of correlation between the dynamics of the RNA contacts
487 at a given gene and the dynamics of the expression of that gene. This observation challenges models
488 proposing that the activation or silencing of a gene may be controlled by a single ncRNA^{89,85,18,78,23}.
489 Instead, our data either indicates that most ncRNAs do not have gene regulatory activity, or favors some of
490 the more complex proposed models, for example, involving coordinated inputs from a ncRNA and the local
491 chromatin environment. One such model, the “junk mail model,” posits that caRNAs interact with chromatin
492 remodeling complexes and keep them poised and in check until other local conditions are satisfied^{53,90}
493 (such as deposition of a specific chromatin modification or binding of a transcription factor). The junk mail
494 model is compatible with our observations. Another possibility, which we termed the “democratic RNA
495 model,” is that the distributed activity of multiple, weakly influential ncRNAs, rather than that of a single,
496 strongly influential ncRNA determines the overall regulatory output of RNA-chromatin interactions at a
497 gene.

498 We found that an increase in interaction frequency between a specific ncRNA and a target gene is
499 more likely to correlate with an increase in target gene expression than one would expect should the
500 ncRNA-gene contacts and the gene expression be uncorrelated with one another. Three scenarios may
501 explain this result. First, this may merely reflect increased accessibility during chromatin activation and
502 higher likelihood to crosslink nearby RNAs. Second, there may be local coregulation of nearby ncRNAs
503 and genes, for instance, through shared regulatory elements. Third, it is possible that the default activities
504 of caRNAs are: i) a decoying of the silencing machinery, as proposed by the junk mail model, in the context
505 of PRC2 eviction⁹¹, or ii) a recruitment of transcription activators such as the CREB-binding protein³⁰.
506 These two effects would also give rise to a positive correlation between caRNA presence at a gene and
507 transcriptional output of this gene.

508 As mentioned above, we did not identify lncRNAs localized at defined genomic targets in *trans*, beyond
509 the interactions explained by the expression levels of these lncRNAs and the distance to their targets. This
510 finding will need to be reconciled with the models proposed for a few ncRNAs, such as DIGIT or RMST,
511 which have been reported to broadly colocalize with BRD3 at endoderm differentiation genes, and SOX2
512 at genes that control pluripotency and neurogenesis, respectively^{78,79,89}. Given that lncRNAs and eRNAs
513 are highly cell state specific^{37,38}, the architecture of the caRNA-chromatin interactome may be qualitatively

514 different and perhaps contain more *trans* interactions in further differentiated cells. Additionally, we cannot
515 exclude the possibility that our analysis missed affinity-driven *trans* interactions due to sequencing depth
516 limitations, in particular for lowly expressed ncRNAs. Thus, deeper sequencing or more powerful statistical
517 frameworks may reveal weak deviations from the model at more loci. However, the fact that our analysis
518 reveals broad differences in the contactome between ES and DE cells gives us confidence that any
519 undetected deviation from the model has to be more subtle than the contactome changes related to cellular
520 differentiation.

521 This work presents a global analysis of caRNA-chromatin interaction and establishes that caRNAs
522 predominately operate locally, through diffusion and genome conformation driven interactions. We
523 anticipate this work will direct the efforts in the non-coding RNA field by providing data-informed priors on
524 the localization of RNAs, and a simple model predicting where non-coding RNAs may act. Future studies to
525 identify the proteins mediating these RNA-chromatin interactions will be necessary to inform the interplay
526 between caRNA and RNA binding proteins in the control of transcription and chromatin state.

527 Methods

528 Cell culture & differentiation

529 **Passaging.** H9 hESCs cells (ES cells) were obtained from Wicell (cell line WA09) and cultured on Corning
530 Matrigel hESC qualified matrix with mTeSR1 medium according to manufacturer's protocols and as
531 described in Loh et al. 2014⁵⁰. Briefly, 6-well plates were prepared with matrigel by adding 1 mL of
532 matrigel (diluted in serum free DMEM/F-12 according to lot dilution factor) to each well and polymerized
533 for 1 hour at room temperature. DMEM/F-12 was aspirated and replaced with 1.5 mL mTeSR1 warmed
534 to room temperature, then 2 μ M of 10 mM ROCK inhibitor (Y27632-Dihydrochloride) was added to each
535 well. H9 hESCs (~3-5 million cell aliquots) were thawed and immediately diluted by dropwise addition of
536 10 mL prewarmed mTeSR1, spun at 200 g for 5 min, and gently resuspended in 1.5 mL mTeSR1. 0.5 mL
537 of cells were added to each well and placed at 37 °C. Media was replaced daily with 2 mL fresh mTeSR1
538 per well. When colonies were ~70% confluent and started to touch each other, cells were passaged as
539 colonies. Each well was washed with 1x PBS, 1 mL of Versene-EDTA was added, and cells were incubated
540 at 37 °C for 5 min. Colonies were detached, broken up with gentle pipetting, and resuspended in mTeSR1
541 at a 1:5 to 1:10 dilution. 0.5 mL of cells was added dropwise to each well containing 1.5 mL mTeSR1 and
542 coated with matrigel prepared as described above (without ROCK inhibitor).

543 **Differentiation into definitive endoderm.** Colonies were seeded from 1:10 dilution on day 0 into four 15 cm
544 dishes with matrigel, two for maintenance as ES cells and two for differentiation into Definitive Endoderm
545 (DE) cells. ES cells were maintained as above with daily mTeSR1 media replacement. For differentiation,
546 cells were treated with 10 μ M ROCK inhibitor on day 0, and their media was replaced on day 1 with
547 DE induction Media A (Gibco Cat# A3062601), and on day 2 with DE induction Media B (Gibco Cat#
548 A3062601). On day 3, cells were harvested for ChAR-seq. In addition to the 15 cm dishes used for
549 ChAR-seq, cells were also seeded and maintained as ES cells or differentiated into DE cells in 6-well plates
550 with poly-L-lysine coated coverslips under matrigel, and collected at the same time for immunofluorescence
551 analysis. Cells were also differentiated in 6-well plates for RNA-seq and ATAC-seq.

552 Immunostaining

553 Cells were cultured in 6-well plates on poly-L-lysine coated coverslips under matrigel and maintained as
554 ES cells or differentiated into DE cells as described above. Cells were washed three times with PBS and
555 fixed with 2% PFA in PBS added directly to the wells for 10 min at room temperature. The PFA solution
556 was aspirated, cells were washed three times with PBS, and permeabilized with 0.1% Triton-X-100 in PBS
557 for 5 min at room temperature. Coverslips were transferred to parafilm-coated staining chambers, washed
558 with PBS, and blocked with Antibody Dilution Buffer (AbDil, 150 mM NaCl, 20 mM Tris-HCl pH 7.4, 0.1%
559 Triton X-100, 2% BSA, 0.1% Sodium Azide) for 30 min at room temperature. Samples were incubated
560 in primary antibody for 30 min at room temperature (Rabbit anti-Nanog 1:500, Goat anti-Sox17 1:1000

561 diluted in AbDil), washed three times with AbDil, and incubated with secondary antibodies conjugated to
562 Goat anti-Rabbit Alexa-647 and Chicken anti-Goat Alexa-555 (1:1000 diluted in AbDil) for 30 min at room
563 temperature. Cells were washed with AbDil three times, stained for 5 min with 10 μ g/mL Hoescht-33342 in
564 PBS, and washed with PBS with 0.1% Triton-X-100 before being mounted (20 mM Tris-HCl pH 8.8, 0.5%
565 p-Phenylenediamine, 90% glycerol) onto slides and sealed with nail polish. Samples were imaged with
566 an IX70 Olympus microscope with a Sedat quad-pass filter set (Semrock) and monochromatic solid-state
567 illuminators. Cells were imaged using a 40x objective. At least 10 images per coverslip were captured
568 using 0.2- μ M *z*-stacks. Maximum intensity projections were processed with CellProfiler (3.1.8) to identify
569 nuclei based on Hoescht signal and to measure the mean intensity of each channel. Histograms of mean
570 nuclear intensity for each marker were plotted in R.

571 **qPCR**

572 For qPCR, RNA was extracted from each well of a 6-well plate containing ES or DE cells (~1 million cells
573 per well) using 1 mL Tripure reagent and according to the manufacturer's protocol. RNA were treated with
574 DNase (TURBO DNase; Ambion) for 1 hour at room temperature followed by isolation with a minElute RNA
575 Cleanup Kit (Qiagen). RNA concentrations were measured by Nanodrop and total RNA integrity assayed
576 using an Agilent Bioanalyzer. All RNAs had a RNA integrity number (RIN) greater than 9.0. 0.5-1 μ g of
577 RNA was reverse-transcribed with random hexamer primers using SuperScript III reverse transcriptase
578 (18080-051; Invitrogen) according to the manufacturer's protocols. First-strand cDNA was diluted 1:10
579 in nuclease free H₂O and amplified using gene-specific primers that had been tested for amplification
580 efficiencies >90% and to amplify a single product. Real-time PCR was performed using the Powerup
581 SYBR Master Mix (ThermoFisher) for 40 cycles (94 °C 15 sec, 55 °C 30 sec, 68 °C, 1 min) on an ABI ViiA
582 7 Real-Time PCR Machine with cycle thresholds (C_{T_s}) determined automatically and with all samples in
583 triplicate. Experimental genes were normalized to the PBGD housekeeping gene, with relative expression
584 levels calculated using the $2^{\Delta\Delta C_T}$ method, and the transcript level fold-change in DE versus ES cells
585 was calculated. If a gene's expression was too low to detect via qPCR, these "undetermined" Ct values
586 were assigned a value of 38 to provide a conservative over-estimate for use in calculation of expression
587 change.

588 **RNA-seq**

589 For RNA-seq, RNA was extracted from each well of a 6-well plate containing ES or DE cells using
590 1 mL Tripure and the Direct-Zol RNA Extraction kit (Zymo Research) according to the manufacturer's
591 instructions. RNA concentrations and quality were assayed as described for qPCR. For each sample, 2.5
592 μ g of RNA was treated with DNase (TURBO DNase; Ambion) for 1 hour at room temperature followed
593 by isolation with a RNA Clean & Concentrator-25 kit (Zymo Research). 1 μ g RNA was converted to
594 ribosomal depleted cDNA libraries ready for sequencing using the TruSeq Stranded Total RNA Library Prep
595 Human/Mouse/Rat kit (Illumina) according to the manufacturer's instructions. Samples were uniquely dual
596 indexed using IDT for Illumina TruSeq RNA UD Indices. The 4 biological replicates from both conditions
597 (ES and DE cells) were pooled and sequenced at low read depth on a MiSeq (2 x PE75) at the Stanford
598 Functional Genomics Facility to assess quality, and later on 1 lane of the HiSeq4000 (2 x PE150) at
599 NovoGene (Sacramento, CA). All reported analysis was generated using the HiSeq dataset.

600 **ATAC-seq**

601 Cells for ATAC-seq were differentiated as described above and collected by dissociating in Versene
602 followed by resuspension in warm mTeSR media. Cells were transferred to 15 mL conical tubes and
603 centrifuged at 1000 RPM for 5 min. The pellet was resuspended in DPBS, cells were counted and
604 immediately processed. ATAC-seq was performed as previously described using the OMNI-ATAC protocol
605 (Corces et al., Nature Methods 2017) with slight modifications. Briefly, ~100K cells were resuspended
606 in 50 μ L cold ATAC-Resuspension Buffer (10 mM Tris-HCl pH 7.4, 10 mM NaCl, 3 mM MgCl₂, 0.01%
607 Digitonin, 0.1% Tween-20, and 0.1% NP40 in water) and incubated on ice. Cells were washed with 1

608 mL cold ATAC-RSB (without NP40 and digitonin), centrifuged at 500 RCF for 10 min at 4 °C. The pellet
609 was resuspended in 50 μ L transposition mixture (2x TD buffer and 2.5 μ L transposase) from the Illumina
610 Nextera DNA Library Prep Kit and incubated at 37 °C for 30 min in a thermomixer at 1000 RPM. Libraries
611 were purified with the DNA Clean & Concentrator-5 Kit (Zymo Research) and PCR amplified with barcoded
612 primers (Buenrostro et al., 2013). Amplification cycle number for each sample was monitored by qPCR
613 to minimize PCR bias. PCR amplified libraries were purified with the MinElute purification kit (Qiagen)
614 and excess primers and large (>1000 bp). DNA fragments were removed by AMPure XP bead selection
615 (Beckman Coulter). Four biological replicates from each cell type (ES and DE) were pooled and sequenced
616 at low read depth on a MiSeq (2 x PE75) at the Stanford Functional Genomics Facility to assess quality
617 and later on 1 lane of the HiSeq4000 (2 x PE150) at NovoGene (Sacramento, CA). All reported analysis
618 was generated using the HiSeq dataset.

619 ChAR-seq library preparation

620 ChAR-seq libraries were prepared according to the published protocol⁴⁷ as briefly described below. All
621 reagents used were RNase-free.

622 **Cell fixation and nuclei.** About 10 million cells were harvested from a 15 cm dish with Versene and fixed in
623 3% formaldehyde for 10 min at room temperature. Formaldehyde was quenched with the addition of 0.6
624 M glycine for 5 min at room temperature then 15 min on ice. Cells were pelleted for 5 min at 500 g at 4 °C,
625 washed with 10 mL ice-cold PBS, and resuspended in ~5-10 mL PBS. Cell concentration was measured
626 and cells were aliquoted in batches of 10 million cells in 1.5 mL tubes. Aliquots were spun for 5 min at
627 500 g at 4 °C, the supernatant was removed, and pellets were flash frozen in liquid nitrogen and stored at
628 –80 °C until library preparation.

629 **Cell lysis and nuclei preparation.** Frozen pellets were resuspended in 500 μ L ice cold lysis buffer (10 mM
630 Tris-HCl pH 8, 10 mM NaCl, 0.2% Igepal-CA630, 1 mM DTT, 1 U/ μ L RNaseOUT, 1x protease inhibitor) and
631 incubated for 15 min on ice. Nuclei were washed (throughout the protocol, “nuclei were washed” indicates
632 the following steps: spinning for 4 min at 2500 g, discarding of supernatant, resuspension and mixing in
633 the indicated wash buffer, spinning for 4 min at 2500 g, and aspiration of the wash buffer) with 500 μ L of
634 lysis buffer without Igepal, RNaseOUT, or Protease Inhibitor, then resuspended in 400 μ L of 0.5% SDS
635 (10 mM Tris-HCl pH 8, 10 mM NaCl, 1 mM DTT, 0.5% SDS, 1 U/ μ L RNaseOUT), and incubated for 10
636 min at 37 °C. SDS was then quenched by adding Triton X-100 to 1.4% final concentration and incubating
637 for 15 min at 37 °C.

638 **In situ biochemistry steps for RNA-DNA proximity ligation.** To fragment RNAs, nuclei were pelleted
639 and resuspended in 150 μ L fragmentation buffer (0.25x T4 RNA ligase buffer, 1 U/ μ L RNaseOUT),
640 and exposed to heat for 4 min at 70 °C. To dephosphorylate RNA 5' ends, nuclei were washed
641 twice (in 800 μ L PBS then 800 μ L 1x RNA ligase buffer, with the first spin omitted for the first
642 wash and PBS added directly to the previous reaction), resuspended in 150 μ L dephosphorylation
643 mix (1x T4 PNK buffer, 1 U/ μ L T4 PNK, 1 U/ μ L RNaseOUT), and incubated for 30 min at
644 37 °C. To perform RNA-bridge ligation, nuclei were washed twice as above and resuspended in
645 200 μ L RNA-bridge ligation mixture [1x T4 RNA ligase buffer, 25 μ M annealed ChAR-seq bridge
646 (top strand: /5rApp/AANNNAACCGGCGTCCAAGGATCTTAATTAAAGTCGCAG/3SpC3/; bottom strand:
647 /5Phos/GATCTGCGACTTAATTAAAGATCCTGGACGCCGG/iBiodT/T; individual strands ordered from
648 IDT DNA), 10 U/ μ L T4KQRNAligase2, 1.5 U/ μ L RNaseOUT, 20% PEG-8000] and incubated overnight
649 at 23 °C on a thermomixer at 900 RPM. To perform first-strand synthesis, nuclei were washed twice as
650 above and resuspended in 250 μ L of first strand synthesis mixture (1x T4 RNA ligase, 8 U/ μ L Bst3.0, 1
651 mM of each dNTP, 1 mM DTT, 1 U/ μ L RNaseOUT), and incubated for 15 min at 23 °C, 10 min at 37 °C,
652 and 20 min at 50 °C. Bst3.0 was inactivated by adding 8 μ L of 0.5 mM EDTA (15 mM final concentration),
653 14 μ L of 1% SDS (0.5% final), and incubating for 10 min at 37 °C. SDS was then quenched with 43 μ L of
654 10% Triton X-100 (1.3% final concentration) for 15 min at 37 °C. Next to perform genomic digestion, nuclei
655 were washed twice and resuspended in 250 μ L of DpnII reaction mixture (1x T4 RNA ligase, 3 U/ μ L DpnII,

656 1 mM DTT, 1 U/ μ L RNaseOUT) overnight at 37 °C on a thermomixer at 900 RPM. DpnII was inactivated
657 in the same manner as Bst3.0 inactivation. SDS was quenched as above. Next, to perform bridge-DNA
658 ligation, nuclei were washed twice and resuspended in 250 μ L of ligation mixture (1x T4 DNA ligase, 10
659 U/ μ L T4 DNA ligase, 1 U/ μ L RNaseOUT) for 4 hours at 23 °C. T4 was inactivated by adding 8 μ L of 0.5 M
660 EDTA (15 mM final concentration). Finally, to perform second strand synthesis, nuclei were washed twice
661 (PBS then 1x cDNA buffer 10 mM Tris-HCl pH 8, 90 mM KCl, 50 mM (NH4)2SO4), and resuspended in
662 250 μ L of second strand synthesis mix (1x cDNA buffer, 0.5 U/ μ L *E. coli* DNA PolI, 0.025 U/ μ L RNaseH, 1
663 mM of each dNTP, 1 mM DTT) for 1.5 hours at 37 °C.

664 **DNA isolation and shearing.** Reverse crosslinking was carried out by adding 31.25 μ L of 10% SDS, 31.25
665 μ L 0.5 M NaCl, 9 μ L of 20 mg/mL proteinase K and incubating overnight at 68 °C. DNA was purified by
666 phenol chloroform extraction, ethanol precipitated, and resuspended in 130 μ L TE (10 mM Tris pH 8, 0.1
667 mM EDTA) buffer. DNA was sheared with a Covaris S220 to target a mean fragment size of ~200 bp (175
668 peak incident power, 10% duty factor, 200 cycles/burst, 180 sec). Fragment size distribution was quality
669 controlled on an Agilent High Sensitivity DNA Bioanalyzer.

670 **Isolation of biotinylated molecules, on-beads adapter ligation, and on-beads PCR.** Molecules containing the
671 biotinylated bridge sequence were isolated using 150 μ L of MyOne Streptavidin T1 dynabeads. To bind
672 bridge containing molecules, beads were washed with 750 μ L tween wash buffer (TWB, 10 mM Tris pH 8,
673 0.5 mM EDTA, 1 M NaCl, 0.05% Tween20) and resuspended in 130 μ L 2x bead binding buffer (10 mM Tris
674 pH 8, 2 M NaCl, 0.5 mM EDTA) and 130 μ L sheared DNA sample, then incubated at room temperature
675 for 15 min with agitation. To remove unbound DNA, beads were washed twice with 750 μ L TWB (with
676 incubation at 50 °C for 2 min with agitation during the first wash), then resuspended in 40 μ L TE buffer.
677 DNA ends were prepared for ligation by adding 7 μ L of NEBNext End Prep Buffer and 3 μ L NEXext
678 End Prep enzyme mix and incubating for 20 min at room temperature and 30 min at 65 °C. Adapters
679 were ligated using NEBNext Ultra II Ligation module according to manufacturer's protocols. Beads were
680 washed twice as above and resuspended in 50 μ L PCR amplification mix (25 μ L 2x NEBNext High Fidelity
681 master mix, 2.5 μ L 10 μ M Universal Primer, 2.5 μ L 10 μ M indexing primer, 20 μ L H₂O). PCR reaction was
682 performed using the following program (1 cycle: 98 °C for 30 sec; 5 cycles: 98 °C for 10 sec, 65 °C for 75
683 sec). Beads were magnetically collected and the supernatant containing amplified DNA was transferred to
684 a clean 1.5 mL microcentrifuge tube. The amplified libraries were purified using magnetic SPRI beads at
685 a ratio of 1:1 and eluted with 31 μ L 10 mM Tris-HCl, pH 8.

686 **Side qPCR & off-bead PCR.** To determine the number of additional cycles of PCR amplification to perform,
687 5 μ L of purified library from on-bead PCR, 6 μ L 2x NEBNext High Fidelity master mix, 0.5 μ L 10 μ M
688 Universal primer, 0.5 μ L 10 μ M indexing primer, and 0.33 μ L 33x SYBR Green were mixed and added
689 to a qPCR well and cycled on an ABI ViiA 7 Real-Time PCR Machine with the following parameters (1
690 cycle: 98 °C for 30 sec; 25 cycles: 98 °C for 10 sec, 65 °C for 75 sec). The number of off-bead PCR
691 cycles to perform was determined by finding the number of cycles such that the fluorescence intensity
692 is about one third the plateau intensity at the PCR saturation. The remaining 25 μ L of the library was
693 combined with 30 μ L 2x NEBNext High Fidelity master mix, 2.5 μ L 10 μ M universal Primer, and 2.5 μ L 10
694 μ M indexing primer. Each sample was then cycled as above for the number of cycles determined by the
695 side qPCR.

696 **Library clean up and sequencing.** To purify the amplified library, high molecular weight fragments were
697 bound to Ampure beads by adding 0.6x volume of the PCR reaction of Ampure beads and collecting
698 the supernatant. Low molecular weight fragments were purified out by adding 0.1875x the volume of
699 the supernatant transferred to obtain a final ratio of 0.9x beads:slurry. DNA was eluted in 33 μ L 10
700 mM Tris pH 8. Library concentration was assessed using a Qubit dsDNA High Sensitivity kit and size
701 distributions were determined using an Agilent High Sensitivity DNA bioanalyzer. Samples were pooled
702 and sequenced on 1 lane of an Illumina HiSeq4000 platform (2x PE150) to assess library quality, then
703 later deeply sequenced on 2 lanes of an Illumina NovaSeq platform at NovoGene (Sacramento, CA). All

704 reported analysis was generated using the NovaSeq dataset. Replicates 1 and 2 of ES and DE ChAR-seq
705 libraries were prepared at different times and each sequenced separately on 1 NovaSeq lane.

706 ChAR-seq data processing and generation of pairs files

707 Demultiplexed fastq files from the ChAR-seq data were processed using a custom Snakemake pipeline
708 (<https://github.com/straightlab/charseq-pipelines>), outputting pairs files containing the RNA
709 and DNA coordinates of each RNA(cDNA)-DNA chimeric read and relevant annotations for each RNA-DNA
710 contact. A summary of the pipeline workflow is depicted in Supplementary Fig. 1. For full details of the
711 processing pipeline, see Supplementary Note 1. Briefly, reads were PCR deduplicated using clumpify.sh
712 v38.84 (BBMap suite), low quality reads ($Q < 30$) were removed, and sequencing adapters were trimmed
713 using Trimmomatic v0.38. Paired-end reads were merged using Pear v0.9.6 when possible and reads
714 containing a single instance of the ChAR-seq bridge sequence were identified using chartools v0.1, a
715 custom ChAR-seq reads preprocessing package released as part of this study (<https://github.com/straightlab/chartools>). Reads were split into a rna.fastq and dna.fastq file corresponding to the
716 sequences of the RNA (cDNA) and DNA side of the chimeric molecule using chartools. Reads with either
717 the RNA or DNA side shorter than 15 bp were removed using chartools, and reads whose RNA side
718 aligned to a rRNA sequence by Bowtie2 were filtered out using Picard. DNA reads were aligned to hg38
719 using Bowtie2, and RNA reads were aligned to hg38 using STAR and Gencode v29 annotations. RNA
720 reads were assigned specific genes using tagtools (<https://github.com/straightlab/tagtools>), a
721 package released as part of this study. pairs files containing for each read the mapping coordinates of
722 the DNA, the RNA, and the most likely gene of origin were produced using chartools pairup function.
723 Separate pairs files were produced for reads whose RNA was annotated by tagtools as exonic, intronic,
724 or intergenic. pairs files were filtered using a bash script to remove multimapping reads and reads with
725 low mapping scores on either the RNA (STAR $Q < 255$) or DNA (Bowtie2 $Q < 40$) side. Reads whose
726 RNA overlapped with the hg38 ENCODE blacklist or that could not be attributed to a single known gene or
727 genomic locus were also removed.

729 RNA-seq data processing

730 RNA-seq reads were processed using a Snakemake pipeline mirroring the ChAR-seq pipeline, but all of
731 the operations related to the DNA-side of the reads were skipped. In brief, demultiplexed fastq files were
732 deduplicated, sequencing adapters were removed, paired mates were merged as described for ChAR-seq
733 reads. Reads that aligned to a rRNA sequence by Bowtie2 were filtered out using Picard. Reads were
734 aligned to hg38 using STAR and were annotated with tagtools using the Gencode V29 gene models. Reads
735 with low mapping scores (STAR $Q < 255$), reads which could not be attributed to a single known gene or
736 a single locus, and reads that overlapped with a locus on the ENCODE black were discarded.

737 ATAC-seq data processing

738 Illumina Nextera Adapters were removed using a custom Python script. Reads were aligned to the hg38
739 using Bowtie2. Duplicates were removed with Picard. Mitochondrial reads or reads with Bowtie2 MAPQ
740 score < 30 were removed using SAMtools. All replicates were similar, so their alignment files were merged
741 to increase library complexity (>100 million mapped reads per cell type) and produce a single bigwig file
742 per cell type used to display the ATAC-seq tracks, and a single bam file to determine ATAC-seq peaks.
743 ATAC-seq peaks were identified in each cell line using HMMRATAC v1.2.10.

744 Chromatin association scores

745 We defined the chromatin association score for RNA i as the log fold difference between the level of
746 RNA i in the chromatin associated RNA transcriptome (measured with the RNA-side of the ChAR-seq
747 reads) and its level in the total RNA transcriptome (measured with total RNA-seq). To estimate
748 the chromatin association score in a way that was robust to small counts and obtain p -values
749 to detect RNAs with meaningful chromatin enrichment, we used DEseq2 with a design formula

750 ~cell + sequencing + cell:sequencing. In this design matrix, the cell covariate represented the
751 cell type and the sequencing covariate indicated whether the sample originated from RNA-seq or
752 ChAR-seq. The interaction term cell:sequencing captured differences in the chromatin association of
753 a given RNA between ES and DE cells. We used the shrunken estimate of the regression coefficient
754 associated with the sequencing covariate as the estimate of the chromatin association score. We
755 computed the chromatin association score in ES and DE cells separately by setting the reference level
756 for the cell covariate to ES and DE, respectively, before running DEseq2. The apeglm method was used
757 to compute the shrunken estimates. We ran DEseq2 using an input count matrix with 16 samples: 2 ES
758 and 2 DE replicates from ChAR-seq and 4 ES and 4 DE replicates from RNA-seq. Gene counts for all
759 Gencode V29 genes and all UTLs identified in this study were included in the input matrix, except those
760 with fewer than 10 counts combined across all 16 samples. Counts from exons and introns of a given gene
761 and from UTLs were input as separate entries (rows) in the matrix. All DESeq2 parameters were set to
762 their default value, except for the sample depth normalization step. For sample depth normalization, we
763 ran the estimateSizeFactors command on a subset of the rows of the count matrix that included only
764 exons of annotated genes with at least 50 counts combined across all 16 samples. Subselecting exonic
765 reads removed length bias due the low representation of introns in the total RNA-seq data compared
766 to the ChAR-seq data. False Discovery Rate (FDR) adjusted *p*-values corresponding to the regression
767 coefficient associated with the sequencing covariate were used to identify genes with significant chromatin
768 enrichment. Genes with an adjusted *p*-value smaller than 0.05 and a chromatin association score either
769 greater than 3 where labeled as chromatin enriched, and those with an adjusted *p*-value smaller than 0.05
770 and a chromatin association score less than -3 were labeled as chromatin depleted. To identify genes with
771 statistically significant changes in their chromatin association score in ES versus DE cells (Fig. 3d), we
772 used the regression coefficient associated with the interaction term cell:sequencing, $LFC_{ES,DE}$ and its
773 corresponding adjusted *p*-value $p_{adj,ES,DE}$. Thresholds used to label such genes were $LFC_{ES,DE} > 0$, and
774 $p_{adj,ES,DE} < 0.05$.

775 Computational interaction with ChAR-seq data

776 For most computational analyses, the filtered pairs files were loaded in python as a chartable python object
777 using the chartools package. Within the object, the interaction data were stored in a sparse matrix with
778 one row per RNA and one column per genomic DpnII site, binned at 10 bp resolution, which could be
779 loaded entirely in RAM. This allowed us to perform computationally efficient indexing operations to select
780 individual RNAs or target genomic loci, plot ChAR-seq maps at various resolutions, produce bigwig files of
781 the binding profile of individual RNAs, and generate the caRNA-gene interactome. All of these operations
782 were performed using methods from the chartools package.

783 De-novo identification and classification of unannotated transcribed loci (UTLs)

784 **Identification of UTLs.** For each ChAR-seq sample, reads whose RNA did not overlap with any gene
785 body in GenecodeV29 in the sense orientation were classified as intergenic by tagtools and their
786 STAR RNA alignments were extracted in a separate bam file. Only RNA reads with a STAR
787 alignment score of $Q = 255$, a cognate DNA read with a Bowtie2 alignment score of $Q > 15$
788 were retained. The reads handling and filtering steps were performed as part of our ChAR-seq
789 reads preprocessing Snakemake pipeline. These bam files were used as an input to StringTie2
790 with parameters `--fr --conservative -u -m 30 -p 4 -A` to produce one gtf file with de-novo
791 gene models for each sample. The sample specific gtf files from the 2 ES and 2 DE ChAR-seq
792 replicates were merged using StringTie2 with parameters `--merge -p 4 -m 30 -c 0 -F 0 -T 0`
793 to produce a final a gtf file `intergenic.merged.gtf` with gene models for the UTL. This
794 gtf file was used to generate a STAR index containing the gene models for the UTLs using
795 command `STAR --runMode genomeGenerate --sjdbGTFfile intergenic.merged.gtf`. A dedicated
796 Snakemake pipeline was run, similar to the full preprocessing pipeline described above, but starting from
797 the tagtools step and using the UTL rather than the gencode gene models (and corresponding STAR
798 indices) to produce pairs files corresponding to RNAs emanating from UTLs.

799 **Classification of UTLs.** Each UTL was assigned 4 metrics or tags. i) We attributed each UTL a dominant
800 Transposable Element (TE) family and a TE-score. For this task, we applied Classification of Ambivalent
801 Sequences using K-mers (CASK)⁸⁶ to the RNA-side of the ChAR-reads. CASK annotates each read with
802 a candidate TE family (if any) based on its k-mer composition analyzed against a database of TE-specific
803 k-mers build using the T2Tv1 genome assembly and T2T-CHM13 repeat annotations. Then, for each UTL,
804 we identified the CASK annotation with the highest representation amongst all the reads (across the 2 ES
805 and 2 DE replicates) mapped to this UTL. We assigned this annotation as the dominant TE family for this
806 UTL and the proportion of reads from this UTL with this specific CASK annotation as its TE-score. ii) If
807 the 5' end of an UTL was within +/- 300 bp of a cis-regulatory element (CRE) active in either ES or DE
808 cells, we annotated this UTL with the closest such CRE and its associated 7-group classification based on
809 the Encode Registry of Regulatory Elements³³ (file ID GRCh38-cCREs.bed). To determine active CRE in
810 ES or DE cells, we selected, amongst the Encode Registry of Regulatory Elements (containing 1,063,878
811 human candidate CREs), those that overlapped with an ATAC-seq peak in that cell line. iii) UTLs whose 5'
812 end were within -200 bp to +100 bp of the 3' end of a GencodeV29 gene body were flagged as candidate
813 "readthrough." iv) UTLs with at least 10% overlap with the antistrand of a GencodeV29 gene body were
814 flagged as candidate "antisense." Finally, these 4 metrics and tags were combined to determine the final
815 UTL classification using the following priority rule: i) UTLs with a dominant TE family of tRNAs and at
816 TE-score greater than 10% were classified as tRNA-derived. ii) Remaining UTLs with a dominant TE
817 family in {snRNA, snoRNA, scaRNA, srpRNA, scRNA, rRNA} and at TE-score greater than 10% were
818 classified as snRNA-derived. iii) Remaining UTLs flagged as candidate readthroughs were classified as
819 readthroughs. iv) Remaining UTLs with a CRE annotation in either ES or DE cells were classified as
820 CRE-derived, and the subtype of CRE was selected from the ES cell annotation if the CRE was active in
821 ES cells, and from DE cell annotation otherwise. v) Remaining UTLs with a TE-score greater than 50%
822 were classified as repeat-derived, with the specific repeat family determined by their dominant TE family.
823 vi) Remaining UTLs flagged as candidate antisense were classified as antisense. vii) All remaining UTL
824 were classified as intergenic.

825 Quantification of the RNA-DNA interactome dynamics

826 To compare the ChAR-seq RNA-DNA contact maps in ES versus DE cells, we repurposed the differential
827 gene expression analysis tool DEseq2⁹². We applied DEseq2 in the interactome space (rather than
828 the transcriptome space, as traditionally done in differential RNA-seq) using the number of ChAR-seq
829 reads linking a specific RNA to a specific DNA locus, hereafter refer to an RNA-DNA interaction, as a
830 separate rows in the input count matrix. We defined a DNA locus as either a 100 kb or 1 Mb genomic
831 window (for Fig. 3), or a region surrounding the TSS of a protein coding gene as defined in the main
832 text (for Fig. 6). The 4 ChAR-seq samples were included as columns of the count matrix. RNA-DNA
833 interactions for which fewer than 2 samples had at least 10 reads were excluded from the count matrix and
834 further analysis. The contact maps from exons, introns, and UTLs were analyzed in independent DESeq2
835 runs. The count matrices were generated in Python directly from the chartable objects that stored the
836 contactome data. These matrices were imported in R and DESeq2 was run with all parameters set to
837 their default values. Log₂ Fold Change differential contacts maps shown in Fig. 3 were generated using
838 the shrunken fold change estimates for each contact as returned by DESeq2. The apegm method was
839 used for shrinkage. This DESeq2 output was loaded into a chartable object in Python for computational
840 handling and visualization tasks using chartools. Bar plots in Fig. 3b were produced using ggplot2 in R
841 after converting the DESeq2 output into dplyr tibbles and applying appropriate transformations.

842 Detection of RNA relocalization events during differentiation.

843 Model 3 in Fig. 3c was tested by comparing the fold change between ES and DE cells for each RNA-DNA
844 interaction with the fold change in total expression of the corresponding RNA in the caRNA transcriptome.
845 To do so, we generated "expression only" contact maps, where the number of contacts between RNA *i* and
846 genomic locus *j* was set equal to the total number of contacts made by RNA *i* in the observed map. For
847 this analysis, genomic loci were defined using a 100 kb tiling partition of the genome. Because in these

848 “expression only” maps, each row i (representing RNA i) is constant across the columns (representing
 849 the 100 kb-wide DNA loci), any information about the localization of individual RNAs is effectively removed
 850 and only the information about the abundance of each RNA is retained. We next applied DEseq2 in
 851 the interactome space as described above, but with the following modifications. First, the count matrix
 852 input to DEseq2 contained 8 samples/columns: the 2 ES and the 2 DE replicates of the observed
 853 contact maps and the 4 corresponding “expression only” maps. Second, we used a design matrix of the
 854 form $\sim \text{cell} + \text{mapType} + \text{cell}:\text{mapType}$, where the `mapType` covariate indicated whether the column
 855 corresponded to an observed ChAR-seq map or an “expression only” map, and the `cell` covariate
 856 indicated whether the column corresponded to a map in ES or DE cells. Third, the count matrix was
 857 prefiltered as above by removing interactions for which fewer than 2 samples had at least 10 reads, except
 858 that only the true observed samples (`mapType=observed`) were considered for the purpose of the filter.
 859 The interaction term `cell:rnaType` captured differences in the ES to DE dynamics in the true maps
 860 compared to the “expression only” maps. All interactions that had an FDR adjusted p -value associated
 861 with the `cell:rnaType` covariate smaller than 0.05 were flagged as “not explained by expression.” Maps
 862 shown in Fig. 3e and labeled as “Differential contacts explained by expression” were generated using the
 863 `apeglm` shrunken estimate of the regression coefficient associated with the `cell` covariate and with the
 864 reference level for `mapType` set to “expressionOnly.” This analysis was performed separately for maps
 865 corresponding to exons, introns, and UTLs.

866 Computation of the *trans*- and *cis*-delocalization scores

867 For full details on the *trans*-delocalization scores please refer to Supplementary Note 2.

trans-delocalization scores. Briefly, we defined the raw *trans*-delocalization score for each RNA as the ratio of the contact density of this RNA on *trans* chromosomes (number of contacts divided by the total length of the *trans* chromosomes) over the contact density of this RNA on its *cis* chromosome. The raw delocalization score was difficult to interpret due to sample-specific biases and dependency in the chromosome of origin and expression (Supplementary Figure 5). To regress out these biases and obtain a score that was comparable across RNAs and samples, we used a generalized linear model (GLM) and an empirical Bayes approach. First, we modeled the total number of *trans*-chromosomal contacts $N_{\text{trans},i}$ for each RNA i as independent Beta Binomial distributions. The Beta Binomial distribution accounts for both the sampling variation and the biological variation across RNAs, and was parametrized with the total number of reads N_i for RNA i , a mean *trans*-contact rate for RNA i π_i , and an overdispersion parameter which we assumed constant across all RNA γ , such that

$$\begin{aligned} \mathbb{E}(N_{\text{trans},i} | N_i) &= \pi_i N_i \\ \text{var}(N_{\text{trans},i} | N_i) &= \pi_i(1 - \pi_i)N_i(1 + (N_i - 1)\gamma) \end{aligned} \tag{1}$$

868 We captured the expression and chromosome biases by using a beta-binomial GLM and by including these
 869 effects as covariates in the GLM. Specifically, we used a logit link function for the mean *trans*-contact rate
 870 π_i of the form

$$\text{logit}(\pi_i) = \eta_{\text{chr},i} + \eta_{\text{expr}} \ln(N_i) \tag{2}$$

871 We next fit the Beta-binomial GLM using our ChAR-seq count data from mRNAs as a training set and
 872 conditioning on the total number of reads N_i for each RNA i .

873 Fitting was performed using the `fit.gamlss` function from the `gamlss` package in R with the beta binomial
 874 family parameter and after loading the count data in a `dplyr` tibble and transforming the table appropriately
 875 for input into the `fit` function. RNAs with fewer than 50 total counts were removed and discarded from
 876 further analysis. Using the fitted beta-binomial GLM, we obtained for each RNA i an estimate for the mean
 877 *trans*-contact rate $\pi_{\text{model},i}$ and an associated Beta Binomial distribution with parameters N_i , $\pi_{\text{model},i}$ and
 878 $\text{gamma}_{\text{model}}$, which we used as an Empirical Bayes prior. We performed a Bayesian update using the true

879 observed number of *trans*-chromosomal contacts for RNA i , thereby obtaining a shrinkage estimate for
880 the *trans*-contact rate $\pi_{\text{post},i}$. We defined the calibrated *trans*-delocalization score for RNA i $\Delta_{\text{trans},i}$ as the
881 \log_2 transformed ratio of the shrinkage estimate over the model prediction:

$$\Delta_{\text{trans},i} = \text{logit}(\pi_{\text{post},i}) - \text{logit}(\pi_{\text{model},i}) \quad (3)$$

882 Delocalization scores were computed independently for each sample, and a final delocalization score for
883 each RNA in each cell state was obtained by averaging the scores over the 2 replicates.

884 ***cis*-delocalization scores.** We defined the RNA travel distance δ for each ChAR-seq read corresponding to
885 a *cis*-chromosomal contact as the distance between the mapping locus of the RNA and the mapping locus
886 of the DNA. *cis*-delocalization scores were defined and computed similarly to the *trans*-delocalization
887 scores, except for the following replacements: the number of *cis*-chromosomal contacts for RNA i was
888 replaced with the number of contacts $N_{\delta < 1\text{Mb},i}$ such that the absolute RNA travel distance was smaller
889 than 1 Mb, and the number of *trans*-chromosomal contacts was replaced with the number of contacts
890 $N_{\delta > 1\text{Mb},i}$ such that the absolute RNA travel distance was greater than 1 Mb. The covariates for the GLM
891 remained unchanged.

892 **Detection of RNAs with extreme delocalization scores**

893 The analysis described below was used for the *trans*-delocalization scores and was performed similarly
894 for the *cis*-delocalization scores. Briefly, for each RNA and each sample, we computed the probability
895 $p_{\text{delocalized},i}$ that a random sample drawn from the posterior distribution of the *trans*-contact rate $\theta_{\text{post},i}$ was
896 larger than a random sample drawn from the GLM trained on the mRNA population. This probability was
897 used as a p -value for identifying *trans*-delocalized RNAs. One p -value was obtained per RNA and per
898 sample, and p -values from replicates were combined using Fisher's method. Multiple hypothesis testing
899 was correction performed using Benjamini Hochberg procedure. RNAs with an adjusted p -value smaller
900 than 0.05 were declared as *trans*-delocalized. To identify RNAs on the other side of the distribution tail
901 (ultra-localized RNAs) $1 - p_{\text{delocalized},i}$ was used, and Fisher's and BH methods were applied similarly. An
902 RNA was declared ultra-localized if the resulting adjusted p -value was smaller than 0.05. All computations
903 were performed in R. For further details please refer to Supplementary Note 2.

904 **Prediction of ChAR-seq contact maps using a generative model**

905 For mathematical details and a detailed discussion on the generative model, please refer to Supplementary
906 Note 3. Briefly, the ChAR-seq dataset can be represented as a set of RNAs from an arbitrarily indexed
907 transcriptome (i.e., RNA i refers to an RNA associated with the i^{th} gene in the transcriptome), and for each
908 RNA i , a set of N_i reads coming from this RNA whose RNA mapping coordinates are $\{r_{i,j}\}_{j=1\dots N_i}$ and
909 DNA mapping coordinates are $\{d_{i,j}\}_{j=1\dots N_i}$. We modeled for each RNA i the probability to observe any
910 particular realization of the DNA mapping coordinates, conditional on knowing i) the set of RNA mapping
911 coordinates and ii) the total number of contacts for this RNA on each chromosome. We modeled the
912 *cis*- and *trans*-chromosomal contacts separately. For *cis*-contacts, we assumed the probability for an
913 RNA emanating from coordinates r to contact locus j with coordinates d_j , is proportional to: i) an RNA
914 independent and DNA locus-dependent bias b_j representing biological and technical variation of RNA
915 localization and detection along the genome and ii) an interaction frequency dependent on the distance
916 between the RNA and the DNA locus. The latter effect captures diffusion and tethering effects at short
917 distances, whereby an RNA is more likely to interact with loci near its transcription site. Under this model,
918 the probability to observe any specific localization pattern for RNA i in *cis* is given by a multinomial
919 distribution of the form:

$$\text{Multinomial} \left(N_{i,\text{cis}}, \propto b_j * \sum_{k \in \mathcal{C}_i} \rho(d_j - r_{i,k}) \right) \quad (4)$$

920 where \mathcal{C}_i is the set of indices amongst the reads from RNA i , for which the DNA-side maps to a locus in *cis*. For *trans*-contacts, we assumed that the probability for any RNA to contact locus j is only proportional
921 to the DNA-bias. Under this model, the probability to observe any specific localization pattern for RNA i
922 on a *trans* chromosome c is given by a multinomial distribution of the form
923

$$\text{Multinomial}\left(N_{i,\text{chr}(i)=c}, b_j\right) \quad (5)$$

924 where $N_{i,\text{chr}(i)=c}$ is the number of contacts made by RNA i on chromosome c .

925 The DNA bias coefficients b_j were estimated using the total coverage at each locus j from all the mRNAs
926 originating from *trans* chromosomes. The distance dependent interaction frequency curve was estimated
927 using the empirical distribution of RNA-DNA travel distance from all the protein coding RNAs. Maps shown
928 across the manuscript and labeled as "model" were obtained by simulating a single realization of the *cis*
929 and *trans* probabilistic models for each RNA in the transcriptome and for each target chromosome. Note
930 that for each RNA, because of the conditional constraints, the total number of contacts on any specific
931 chromosome are always equal in the simulated data and in the observed data. All simulations were
932 performed in python as described in Supplementary Note 4, and the resulting maps were loaded in memory
933 as chartables using chartools for analysis and plotting purposes.

934 **Detection of RNA-DNA contacts not predicted by the generative model**

935 To compare the true observed ChAR-seq RNA-DNA contact maps to those predicted by the generative
936 model, we applied DEseq2 in the interactome space as described in the section "Quantification of
937 the RNA-DNA interactome dynamics" with the following modifications. First, the count matrix input to
938 DEseq2 contained 8 samples/columns : the 2 ES and the 2 DE replicates of the true "observed" contact
939 maps, and the 4 corresponding "model" maps, obtained by a single simulation of the generative model.
940 Second, the design matrix was set to $\sim \text{cell} + \text{observedORmodel} + \text{cell:observedORmodel}$, where
941 the `observedORmodel` covariate indicated whether the column corresponded to "observed" or "model"
942 ChAR-seq map. Third, the count matrix was prefiltered by removing interactions for which fewer than 2
943 samples amongst the "observed" samples had at least 10 reads. The interaction term `cell:rnaType`
944 captured differences between the observed and modeled data that were specific to either ES to DE
945 cells. All interactions whose `apeglm` shrunken estimate of the regression coefficient associated with the
946 `observedORmodel` covariate was greater than $\log_2(1.3)$ and had an FDR adjusted p -value smaller than 0.0
947 5 were flagged as "not explained by model." We computed the regression coefficient associated with the
948 `observedORmodel` and its p -value in ES and DE cells separately, by setting the reference level for the `cell`
949 covariate to ES and DE, respectively, before running DEseq2. This analysis was performed separately for
950 maps corresponding to exons, introns, and UTLs. Maps shown in Fig. 5d-h, and Fig. 6b labeled as "model"
951 or "mod" were generated using the `apeglm` shrunken estimate of the regression coefficient associated
952 with the `observedORmodel` covariate. The DESeq2 outputs were loaded into a chartable object in Python
953 using chartools for visualization tasks. Bar and line plots in Fig. 5e were produced using ggplot2 in R
954 after converting the DESeq2 output into dplyr tibbles and applying appropriate transformations.

955 **External data used in this study**

956 Hi-C data in Fig. 5 were loaded in HiGlass from the Krietenstein et al. 2019 (H1 hESCs) dataset⁹³,
957 visualized at 2kb resolution after ICE normalization, and manually aligned with the ChAR-seq, ATAC-seq,
958 H3K27ac and H3K4me3 tracks plotted in IGV based on their genomic coordinates. H3K27ac and
959 K3K4me3 tracks in Fig. 2b and Fig. 5g were generated using ChIP-seq data in H7 hESCs cells and H7
960 cells differentiated into definitive endoderm from GSE127202⁵⁰.

961 **Data and code availability**

962 All ChAR-seq, RNA-seq and ATAC-seq sequencing data generated as part of this study are available
963 by request and will be made publicly available on GEO upon publication. Packages released as part of

964 this study and Snakemake pipelines used to preprocess the ChAR-seq and RNA-seq data are available
965 on github at the specific repositories described above. All data analysis code and code to generate the
966 figures are available by request and will be available on github upon publication.

967 Acknowledgements

968 This research was supported by National Institutes of Health (NIH) grant NIH R01 HG009909 to WJG
969 and AFS. OKS was supported by the Training Grant NIH T32-GM113854-02 and NSF-GRFP, and by the
970 Stanford Center for Systems Biology Seed Grant Award. Some of the computing for this project was
971 performed on the Sherlock cluster. We would like to thank Stanford University and the Stanford Research
972 Computing Center for providing computational resources and support that contributed to these research
973 results. We thank Viviana Risca for assistance with the protocols and helpful discussions, and Ali Shariati
974 for assistance with cell culture. We thank the members of the Straight lab for advice and feedback on the
975 manuscript.

976 Contributions

977 CL, OKS, DJ, WJG and AFS conceptualized the study. OKS, DJ, and KAF performed cell culture work.
978 DJ prepared RNA-seq and ATAC-seq libraries, and processed the ATAC-seq data. CL, OKS and DJ
979 performed the ChAR-seq experiments and library preparation. CL developed the concepts related to RNA
980 localization patterns, developed and wrote the computational tools to analyze the data, and performed
981 the computational and statistical analysis. OKS, DJ and KAF helped with data analysis. CL performed
982 visualizations. KAF helped with figures. CL wrote the original draft of the manuscript. CL, OKS, DJ,
983 KAF, WJG and AFS reviewed and edited the manuscript. WJG and AFS provided resources and acquired
984 funding. AFS supervised the study.

985 Competing Interests

986 W.J.G. is a consultant and equity holder for 10x Genomics, Guardant Health, Quantapore and Ultima
987 Genomics, Lamar Health, and cofounder of Protillion Biosciences, and is named on patents describing
988 ATAC-seq.

989 References

- 990 1. Forrest, A. R. *et al.* FANTOM consortium and the RIKEN PMI and CLST (DGT): a promoter-level mammalian expression
991 atlas. *Nature* **507**, 462–470 (2014).
- 992 2. Engreitz, J. M., Ollikainen, N. & Guttman, M. Long non-coding RNAs: spatial amplifiers that control nuclear structure and
993 gene expression. *Nat. Rev. Mol. Cell Biol.* **17**, 756–770 (2016).
- 994 3. Statello, L., Guo, C.-J., Chen, L.-L. & Huarte, M. Gene regulation by long non-coding RNAs and its biological functions. *Nat. Rev. Mol. Cell Biol.* **22**, 96–118 (2021).
- 995 4. Yin, Y. *et al.* U1 snRNP regulates chromatin retention of noncoding RNAs. *Nature* **580**, 147–150 (2020).
- 996 5. Engreitz, J. M. *et al.* RNA-RNA interactions enable specific targeting of noncoding RNAs to nascent Pre-mRNAs and
997 chromatin sites (2014).
- 998 6. Creamer, K. M., Kolpa, H. J. & Lawrence, J. B. Nascent RNA scaffolds contribute to chromosome territory architecture and
999 counter chromatin compaction. *Mol. Cell* **81**, 3509–3525.e5 (2021).
- 1000 7. Hall, L. L. *et al.* Stable C0T-1 repeat RNA is abundant and is associated with euchromatic interphase chromosomes. *Cell*
1001 **156**, 907–919 (2014).
- 1002 8. Kim, T.-K. *et al.* Widespread transcription at neuronal activity-regulated enhancers. *Nature* **465**, 182–187 (2010).
- 1003 9. Mousavi, K. *et al.* eRNAs promote transcription by establishing chromatin accessibility at defined genomic loci. *Mol. Cell*
1004 **51**, 606–617 (2013).
- 1005 10. Rahnamoun, H. *et al.* RNAs interact with BRD4 to promote enhanced chromatin engagement and transcription activation.
1006 *Nat. Struct. Mol. Biol.* **25**, 687–697 (2018).
- 1007 11. Jachowicz, J. W. *et al.* LINE-1 activation after fertilization regulates global chromatin accessibility in the early mouse embryo
1008 (2018).
- 1009 12. Burton, A. *et al.* Heterochromatin establishment during early mammalian development is regulated by pericentromeric RNA
1010 and characterized by non-repressive H3K9me3. *Nat. Cell Biol.* **22**, 767–778 (2020).
- 1011 13. Conte, C., Dastugue, B. & Vaury, C. Promoter competition as a mechanism of transcriptional interference mediated by
1012 retrotransposons. *EMBO J.* **21**, 3908–3916 (2002).

1014 14. Carter, T. A. *et al.* Mosaic cis-regulatory evolution drives transcriptional partitioning of HERVH endogenous retrovirus in the
1015 human embryo. *Elife* **11** (2022).

1016 15. Werner, M. S. *et al.* Chromatin-enriched lncRNAs can act as cell-type specific activators of proximal gene transcription. *Nat.*
1017 *Struct. Mol. Biol.* **24**, 596–603 (2017).

1018 16. Werner, M. S. & Ruthenburg, A. J. Nuclear fractionation reveals thousands of Chromatin-Tethered noncoding RNAs adjacent
1019 to active genes (2015).

1020 17. Engreitz, J. M. *et al.* The xist lncRNA exploits three-dimensional genome architecture to spread across the X chromosome. *Science*
1021 **341**, 1237973 (2013).

1022 18. Pandey, R. R. *et al.* Kcnq1ot1 antisense noncoding RNA mediates Lineage-Specific transcriptional silencing through
1023 Chromatin-Level regulation. *Mol. Cell* **32**, 232–246 (2008).

1024 19. Korostowski, L., Sedlak, N. & Engel, N. The kcnq1ot1 long Non-Coding RNA affects chromatin conformation and expression
1025 of kcnq1, but does not regulate its imprinting in the developing heart. *PLoS Genet.* **8**, e1002956 (2012).

1026 20. Schaukowitch, K. *et al.* Enhancer RNA facilitates NELF release from immediate early genes. *Mol. Cell* **56**, 29–42 (2014).

1027 21. Shii, L., Song, L., Maurer, K., Zhang, Z. & Sullivan, K. E. SERPINB2 is regulated by dynamic interactions with pause-release
1028 proteins and enhancer RNAs. *Mol. Immunol.* **88**, 20–31 (2017).

1029 22. Huang, Z. *et al.* The corepressors GPS2 and SMRT control enhancer and silencer remodeling via eRNA transcription during
1030 inflammatory activation of macrophages. *Mol. Cell* **81**, 953–968.e9 (2021).

1031 23. Tsai, P.-F. *et al.* A Muscle-Specific enhancer RNA mediates cohesin recruitment and regulates transcription in trans. *Mol.*
1032 *Cell* **71**, 129–141.e8 (2018).

1033 24. Nozawa, R.-S. *et al.* SAF-A regulates interphase chromosome structure through oligomerization with Chromatin-Associated
1034 RNAs. *Cell* **169**, 1214–1227.e18 (2017).

1035 25. Marasca, F. *et al.* LINE1 are spliced in non-canonical transcript variants to regulate T cell quiescence and exhaustion. *Nat.*
1036 *Genet.* **54**, 180–193 (2022).

1037 26. Xiao, R. *et al.* Pervasive Chromatin-RNA binding protein interactions enable RNA-Based regulation of transcription. *Cell*
1038 **178**, 107–121.e18 (2019).

1039 27. He, C. *et al.* High-Resolution mapping of RNA-Binding regions in the nuclear proteome of embryonic stem cells. *Mol. Cell*
1040 **64**, 416–430 (2016).

1041 28. Holz-Schietinger, C. & Reich, N. O. RNA modulation of the human DNA methyltransferase 3A. *Nucleic Acids Res.* **40**,
1042 8550–8557 (2012).

1043 29. Johnson, W. L. *et al.* RNA-dependent stabilization of SUV39H1 at constitutive heterochromatin. *Elife* **6** (2017).

1044 30. Bose, D. A. *et al.* RNA binding to CBP stimulates histone acetylation and transcription. *Cell* **168**, 135–149.e22 (2017).

1045 31. Saldaña-Meyer, R. *et al.* RNA interactions are essential for CTCF-Mediated genome organization. *Mol. Cell* **76**, 412–422.e5
1046 (2019).

1047 32. Ponting, C. P. & Haerty, W. Genome-Wide analysis of human long noncoding RNAs: A provocative review. *Annu. Rev.*
1048 *Genomics Hum. Genet.* (2022).

1049 33. ENCODE Project Consortium *et al.* Expanded encyclopaedias of DNA elements in the human and mouse genomes. *Nature*
1050 **583**, 699–710 (2020).

1051 34. Kung, J. T. Y., Colognori, D. & Lee, J. T. Long noncoding RNAs: past, present, and future. *Genetics* **193**, 651–669 (2013).

1052 35. Arner, E. *et al.* Transcribed enhancers lead waves of coordinated transcription in transitioning mammalian cells. *Science*
1053 **347**, 1010–1014 (2015).

1054 36. Andersson, R. *et al.* An atlas of active enhancers across human cell types and tissues. *Nature* **507**, 455–461 (2014).

1055 37. Melé, M. *et al.* Human genomics. the human transcriptome across tissues and individuals. *Science* **348**, 660–665 (2015).

1056 38. Jiang, S. *et al.* An expanded landscape of human long noncoding RNA. *Nucleic Acids Res.* **47**, 7842–7856 (2019).

1057 39. Wu, H. *et al.* Tissue-specific RNA expression marks distant-acting developmental enhancers. *PLoS Genet.* **10**, e1004610
1058 (2014).

1059 40. Deveson, I. W., Hardwick, S. A., Mercer, T. R. & Mattick, J. S. The dimensions, dynamics, and relevance of the mammalian
1060 noncoding transcriptome. *Trends Genet.* **33**, 464–478 (2017).

1061 41. De Santa, F. *et al.* A large fraction of extragenic RNA pol II transcription sites overlap enhancers. *PLoS Biol.* **8**, e1000384
1062 (2010).

1063 42. Mercer, T. R. *et al.* Targeted RNA sequencing reveals the deep complexity of the human transcriptome. *Nat. Biotechnol.* **30**,
1064 99–104 (2011).

1065 43. Miyata, K. *et al.* Pericentromeric noncoding RNA changes DNA binding of CTCF and inflammatory gene expression in
1066 senescence and cancer. *Proc. Natl. Acad. Sci. U. S. A.* **118** (2021).

1066 44. de Goede, O. M. *et al.* Population-scale tissue transcriptomics maps long non-coding RNAs to complex disease. *Cell* **184**,
1068 2633–2648.e19 (2021).

1069 45. Li, J. *et al.* ncRNA-eQTL: a database to systematically evaluate the effects of SNPs on non-coding RNA expression across
1070 cancer types. *Nucleic Acids Res.* **48**, D956–D963 (2020).

1071 46. Goldfarb, K. C. & Cech, T. R. Targeted CRISPR disruption reveals a role for RNase MRP RNA in human preribosomal RNA
1072 processing. *Genes Dev.* **31**, 59–71 (2017).

1073 47. Limouse, C., Jukam, D., Smith, O. K., Fryer, K. A. & Straight, A. F. Mapping Transcriptome-Wide and Genome-Wide
1074 RNA-DNA contacts with Chromatin-Associated RNA sequencing (ChAR-seq). *Methods Mol. Biol.* **2161**, 115–142 (2020).

1075 48. Bell, J. C. *et al.* Chromatin-associated RNA sequencing (ChAR-seq) maps genome-wide RNA-to-DNA contacts. *Elife* **7**
1076 (2018).

1077 49. Jukam, D. *et al.* Chromatin-associated RNA sequencing (ChAR-seq). *Curr. Protoc. Mol. Biol.* **126**, e87 (2019).

1078 50. Loh, K. M. *et al.* Efficient endoderm induction from human pluripotent stem cells by logically directing signals controlling
1079 lineage bifurcations. *Cell Stem Cell* **14**, 237–252 (2014).

1080 51. Van Nostrand, E. L. *et al.* A large-scale binding and functional map of human RNA-binding proteins. *Nature* **583**, 711–719
1081 (2020).

1082 52. Bao, X. *et al.* Capturing the interactome of newly transcribed RNA. *Nat. Methods* **15**, 213–220 (2018).

1083 53. Kaneko, S., Son, J., Bonasio, R., Shen, S. S. & Reinberg, D. Nascent RNA interaction keeps PRC2 activity poised and in

1084 check. *Genes Dev.* **28**, 1983–1988 (2014).

1085 54. Quinodoz, S. A. et al. RNA promotes the formation of spatial compartments in the nucleus. *Cell* **184**, 5775–5790.e30 (2021).

1086 55. Li, X. et al. GRID-seq reveals the global RNA–chromatin interactome. *Nat. Biotechnol.* **35**, 940–950 (2017).

1087 56. Sridhar, B. et al. Systematic mapping of RNA-Chromatin interactions in vivo. *Curr. Biol.* **27**, 602–609 (2017).

1088 57. Bonetti, A. et al. RADICL-seq identifies general and cell type-specific principles of genome-wide RNA-chromatin interactions. *Nat. Commun.* **11**, 1018 (2020).

1089 58. Belton, J.-M. et al. Hi-C: a comprehensive technique to capture the conformation of genomes. *Methods* **58**, 268–276 (2012).

1090 59. Cremer, T. & Cremer, M. Chromosome territories. *Cold Spring Harb. Perspect. Biol.* **2**, a003889 (2010).

1091 60. West, J. A. et al. The long noncoding RNAs NEAT1 and MALAT1 bind active chromatin sites. *Mol. Cell* **55**, 791–802 (2014).

1092 61. Patrat, C., Ouimet, J.-F. & Rougeulle, C. X chromosome inactivation in human development. *Development* **147** (2020).

1093 62. Kovaka, S. et al. Transcriptome assembly from long-read RNA-seq alignments with StringTie2. *Genome Biol.* **20**, 278 (2019).

1094 63. Agostini, F., Zagalak, J., Attig, J., Ule, J. & Luscombe, N. M. Intergenic RNA mainly derives from nascent transcripts of known genes. *Genome Biol.* **22**, 136 (2021).

1095 64. Vilborg, A., Passarelli, M. C., Yario, T. A., Tycowski, K. T. & Steitz, J. A. Widespread inducible transcription downstream of human genes. *Mol. Cell* **59**, 449–461 (2015).

1096 65. Seila, A. C. et al. Divergent transcription from active promoters. *Science* **322**, 1849–1851 (2008).

1097 66. Preker, P. et al. RNA exosome depletion reveals transcription upstream of active human promoters. *Science* **322**, 1851–1854 (2008).

1098 67. Hopper, A. K., Pai, D. A. & Engelke, D. R. Cellular dynamics of tRNAs and their genes. *FEBS Lett.* **584**, 310–317 (2010).

1099 68. Tripathi, V. et al. The nuclear-retained noncoding RNA MALAT1 regulates alternative splicing by modulating SR splicing factor phosphorylation. *Mol. Cell* **39**, 925–938 (2010).

1100 69. Zhang, X., Hamblin, M. H. & Yin, K.-J. The long noncoding RNA malat1: Its physiological and pathophysiological functions. *RNA Biol.* **14**, 1705–1714 (2017).

1101 70. Prasanth, K. V. et al. Nuclear organization and dynamics of 7SK RNA in regulating gene expression. *Mol. Biol. Cell* **21**, 4184–4196 (2010).

1102 71. Flynn, R. A. et al. 7SK-BAF axis controls pervasive transcription at enhancers. *Nat. Struct. Mol. Biol.* **23**, 231–238 (2016).

1103 72. Nagpal, N. & Agarwal, S. Telomerase RNA processing: Implications for human health and disease. *Stem Cells* (2020).

1104 73. Lygerou, Z., Allmang, C., Tollervey, D. & Séraphin, B. Accurate processing of a eukaryotic precursor ribosomal RNA by ribonuclease MRP in vitro. *Science* **272**, 268–270 (1996).

1105 74. Lan, P. et al. Structural insight into precursor ribosomal RNA processing by ribonuclease MRP. *Science* **369**, 656–663 (2020).

1106 75. Guerrier-Takada, C., Gardiner, K., Marsh, T., Pace, N. & Altman, S. The RNA moiety of ribonuclease P is the catalytic subunit of the enzyme. *Cell* **35**, 849–857 (1983).

1107 76. Jarrous, N. Roles of RNase P and its subunits. *Trends Genet.* **33**, 594–603 (2017).

1108 77. Hacisuleyman, E. et al. Topological organization of multichromosomal regions by the long intergenic noncoding RNA firre. *Nat. Struct. Mol. Biol.* **21**, 198–206 (2014).

1109 78. Ng, S.-Y., Bogu, G. K., Soh, B. S. & Stanton, L. W. The long noncoding RNA RMST interacts with SOX2 to regulate neurogenesis. *Mol. Cell* **51**, 349–359 (2013).

1110 79. Daneshvar, K. et al. lncRNA DIGIT and BRD3 protein form phase-separated condensates to regulate endoderm differentiation. *Nat. Cell Biol.* **22**, 1211–1222 (2020).

1111 80. Zhang, Y. et al. Model-based analysis of ChIP-Seq (MACS). *Genome Biol.* **9**, R137 (2008).

1112 81. Chen, Y. et al. Mapping 3D genome organization relative to nuclear compartments using TSA-Seq as a cytological ruler (2018).

1113 82. Rao, S. S. P. et al. A 3D map of the human genome at kilobase resolution reveals principles of chromatin looping. *Cell* **159**, 1665–1680 (2014).

1114 83. Dixon, J. R. et al. Topological domains in mammalian genomes identified by analysis of chromatin interactions. *Nature* **485**, 376–380 (2012).

1115 84. Lieberman-Aiden, E. et al. Comprehensive mapping of long-range interactions reveals folding principles of the human genome. *Science* **326**, 289–293 (2009).

1116 85. Tsai, M.-C. et al. Long noncoding RNA as modular scaffold of histone modification complexes. *Science* **329**, 689–693 (2010).

1117 86. Hoyt, S. J. et al. From telomere to telomere: The transcriptional and epigenetic state of human repeat elements. *Science* **376**, eabk3112 (2022).

1118 87. Quinodoz, S. A. et al. Higher-Order inter-chromosomal hubs shape 3D genome organization in the nucleus. *Cell* **174**, 744–757.e24 (2018).

1119 88. Jain, A. K. et al. LncPRESS1 is a p53-regulated LncRNA that safeguards pluripotency by disrupting SIRT6-Mediated de-acetylation of histone H3K56. *Mol. Cell* **64**, 967–981 (2016).

1120 89. Daneshvar, K. et al. DIGIT is a conserved long noncoding RNA that regulates GSC expression to control definitive endoderm differentiation of embryonic stem cells. *Cell Rep.* **17**, 353–365 (2016).

1121 90. Davidovich, C. & Cech, T. R. The recruitment of chromatin modifiers by long noncoding RNAs: lessons from PRC2 (2015).

1122 91. Davidovich, C., Zheng, L., Goodrich, K. J. & Cech, T. R. Promiscuous RNA binding by polycomb repressive complex 2. *Nat. Struct. Mol. Biol.* **20**, 1250–1257 (2013).

1123 92. Love, M. I., Huber, W. & Anders, S. Moderated estimation of fold change and dispersion for RNA-seq data with DESeq2. *Genome Biol.* **15**, 550 (2014).

1124 93. Krietenstein, N. et al. Ultrastructural details of mammalian chromosome architecture. *Mol. Cell* **78**, 554–565.e7 (2020).